Research article

Visible-light-activated antibacterial and antipollutant properties of biocompatible Cu-doped and Ag-decorated TiO$_2$ nanoparticles

Panagiotis Tzevelekidis [a,1], Maria Theodosiou [a,b,1], Athina Papadopoulou [a,b], Elias Sakellis [b,c], Nikos Boukos [b], Alexandros K. Bikogiannakis [d], Georgios Kyriakou [d], Eleni K. Efthimiadou [a,*], Christiana A. Mitsopoulou [a,**]

[a] Inorganic Chemistry Laboratory, Department of Chemistry, National and Kapodistrian University of Athens, Panepistimiopolis, 15771, Zografou, Greece
[b] Institute of Nanoscience and Nanotechnology, National Center of Scientific Research "Demokritos", Agia Paraskevi, 15341, Greece
[c] Section of Condensed Matter Physics, Department of Physics, National and Kapodistrian University of Athens, Athens, 15784, Greece
[d] Department of Chemical Engineering, University of Patras, Caratheodory 1, Patras, 26504, Greece

ABSTRACT

Optical and photocatalytic restrictions of anatase TiO$_2$ nanoparticles (Nps) limit their potential applications, as antipollutant and antibacterial agents for sanitary applications, to the UV spectral region. While modification with transition metals extends the absorption capacity to the visible light spectrum, often undermines the photocatalysts' biocompatibility due to toxic ion leaching. In this study, we synthesized Cu-doped and Ag-decorated TiO$_2$ photocatalysts by employing solvothermal ($_A$TiO$_2$:Cu) and sol-gel synthetic procedures ($_B$TiO$_2$:Ag), respectively. We acquired TiO$_2$ Nps modified with three percentages of either Cu or Ag content, to examine the potential differentiation of their structural, photocatalytic, and biological impact. Comprehensive structural characterization supports the prevailing anatase crystalline structure of bare and modified titania nanostructures, while morphological differences are demonstrated among the different samples. Optical response in the visible region of $_A$TiO$_2$:Cu Nps stems from band gap narrowing and lattice-defect generation, while plasmonic effects are at play for $_B$TiO$_2$:Ag Nps. Their photocatalytic potential under visible light irradiation, originated from low-energy LED lamps commonly found in indoor spaces, was verified after monitoring the successful enhancement of methylene blue (MB) degradation rate. Safety assessment on immortalized healthy human keratinocyte cell line (HaCaT) revealed their biocompatibility up to a certain concentration, while reactive oxygen species (ROS) production was intensified after light irradiation. The visible-light-induced photocatalytic-driven antibacterial activity was confirmed against both gram-positive *Staphylococcus aureus* and gram-negative *Escherichia coli*.

1. Introduction

Mitigation of indoor sanitation is increasingly demanded due to climate change and overpopulation in urban areas favouring microbial growth [1]. As we spend 90 % of our daily lives indoors, environmental pollution and microbial infected surfaces are of high-risk imposing life-threatening diseases [2]. Conventional cleaning methods aren't the answer to the problem anymore, due to their biological and ecological toxicity [3]. Incorporation of antipollution and antimicrobial agents on surfaces, i.e. in paints and coatings of those surfaces, imposes a sustainable solution to address this problem [4]. The main constituent in such formulations were, at first, toxic common inorganic biocides but were then replaced by eco-friendly organic biocides, which were found to imposed formulation instability stability problems in paints and coatings [5]. Then nanotechnology became handy, as nanomaterials were proven to possess exceptional mechanical and chemical characteristics, while adding extra properties due to their exceptionally small size. In a recent review study, TiO_2 Nps as well as Ag and Cu containing nanocomposites, are highlighted in several experimental and real-life applications as antibiofouling agents on different types of surfaces with remarkable results [6]. TiO_2 specifically, has been employed as a white pigment for several decades, but at the beginning of 21st century, nanosized TiO_2 has been effectively incorporated in construction materials due its photocatalytic properties [7,8]. TiO_2, referred to as titania, has been extensively studied as a support for metal catalysts [9]and mainly as a photoactive material. Since the discovery of water photooxidation on a TiO_2 electrode [10], known as the Honda-Fujishima effect, the inception of TiO_2's use as a photocatalyst has been tested in numerous applications; photocatalytic water splitting under solar light [11] photocatalytic mineralization of toxic pollutants from atmosphere and water, and photocatalytic degradation of organic pollutants [12]. Titania has also been explored for biomedical applications such as antibacterial coatings, wound healing, and drug delivery systems, mainly due to its low toxicity and biocompatibility [13–19].

The photocatalytic activity of nanostructured TiO_2 is affected by its crystallinity, shape, size, and level of aggregation. Titania exists in three crystalline structures: anatase, rutile, and brookite. Anatase exhibits superior photocatalytic activity compared to rutile [20], whilst limited research exists on the photocatalytic properties of metastable brookite due to synthetic challenges for acquiring a pure crystalline phase, i.e., the absence of anatase. Photocatalytic performance, of these crystalline phases, strongly depends on the electronic configuration and band structures [21]. The higher density of electronic states in the conduction band of anatase, facilitates efficient charge separation leading to enhanced photocatalytic activity [22]. However, anatase TiO_2 has major optical limitations stemming from a relatively wide bandgap (~3.2 eV), which restricts its absorption within the UV range, accounting for only 5 % of solar light [23,24]. Thus, the utilization of TiO_2 as a photocatalyst is rendered inefficient for ambient light applications.

Several approaches have been explored to extend the absorption spectral range of TiO_2 Nps, including doping with foreign ions or atoms (Cu^{2+}, Mn^{2+}, Ag^+, B, N, and S) [25–33], surface decoration with plasmonic nanoparticles (Au, Pt, Ag) [33–37], coupling with other semiconductors (CuO, Cu_2O, g-CN) [38–42], and dye photosensitization [43–45].

Copper (Cu) and silver (Ag) have shown effective extension of TiO_2's optical capacity towards the visible spectral region, while also contributing to the separation of the photogenerated charge carriers Copper (Ar = 29), with a ground state electronic configuration of $[Ar]3d^{10}4s^1$, a first-row transition metal, has three accessible oxidation states (Cu^+, Cu^{2+}, Cu^{3+}). The introduction of these ions, and especially Cu^+ and Cu^{2+}, into the crystal lattice of TiO_2 Nps, can induce localized states within the bandgap, boosting visible light absorption-related properties. Coupling with narrow bandgap semiconductors CuO (~1.2 eV) [46] and Cu_2O (~2.2 eV) [47] can facilitate charge transfer and limit the recombination of excitons. Furthermore, Cu and it's oxides are known antimicrobial agents, via their intrinsic reactive oxygen species (ROS) evolution mechanism [48–50]. Thus, doping or forming heterojunctions of TiO_2 with Cu ions are promising ways to improve TiO_2's photocatalytic-driven antimicrobial activity.

Silver, predominantly existing in the Ag^+ oxidation state due to its atomic structure $[Kr] 5s^1 4 d^{10}$, has also been effectively incorporated into TiO_2 in various studies to expand its photocatalytic efficiency towards the visible spectrum. Silver ions have long been recognized for their potent antimicrobial properties and when incorporated into the TiO_2 matrix, they may be released rendering TiO_2 nanoparticles a formidable agent against a spectrum of pathogens [51]. Research focus has shifted to nanoparticulate Ag^0 (Ag Nps) due to its intrinsic properties; high surface area for catalytic reactions, localized surface plasmon resonance (LSPR) effect, and enhanced stability. Despite its non-conventional semiconductor bandgap, the LSPR of Ag Nps is vital for their optical response, involving light absorption boost, scattering, and local electromagnetic field enhancement, particularly in photocatalysis applications [52,53]. The antibacterial effect of Ag Nps can be attributed to the sustained release of Ag^+ which follows different biochemical paths, like adhesion and disruption of the cellular membrane as well as oxidative stress via extracellular or intracellular ROS production [54–57]. Safety assessment of Ag Nps against Ag^+, on human hepatoma cells, demonstrated a 10-fold decrease of IC50 values, indicating increased biocompatibility of the nanoparticulate form compared to the ionic state of silver [58]. Synthesis of Ag Nps decorated TiO_2 nanostructures has been reported by either mixing of pre-synthesized TiO_2 Nps with Ag precursors in a reducing environment, or by deposition of Ag Nps on TiO_2 substrates and even solvothermal techniques, financially limiting their potential for commercial production [59].

To date, several studies have reported the light-activated antibacterial and antipollutant properties of Cu and Ag modified TiO_2 nanoparticles. Nikhila et al. synthesized Cu and Ag decorated TiO_2 mesoporous nanocuboids with exposed facets which exhibited increased photodegradation rate in the photocatalytic decomposition of MB under the illumination of UV–Visible light [60]. The main active species of the transition metals contributing to the increased photocatalytic ability of the nanostructures where CuO and Cu_2O oxides and metallic Ag respectively. Recently, it has been shown that the incorporation of Ag nanoparticles into a ternary NiO/Ag/TiO_2 photocatalyst significantly enhanced the MB degradation rate under visible light illumination, far outperforming bare TiO_2 [61]. Wei et al. employed a multi-step procedure for the synthesis of Ag and Cu decorated anatase titania nanoparticles with enhanced antibacterial activity under the illumination of pure visible light originated from a solar simulator with a UV cut-off filter [62].

However, the implemented approaches mainly involve activation under UV and UV–Vis light or high-energy solar-simulator Xe

lamps paired with UV-cut off filters whereas the effect of pure visible light ($\lambda > 400$ nm) from low-energy indoor lamps remains relatively understudied [63–70]. Furthermore, the aforementioned studies extensively evaluate the photocatalytic properties of the synthesized nanoparticles, which, however, need to meet the appropriate biological requirements to be considered for further indoor, real-life applications. To our knowledge, no other studies have reported a combination of biocompatibility and visible light photo-activation for Cu- and Ag-modified TiO_2 nanoparticles. Herein, two robust one-pot and easily up-scalable synthetic procedures were developed for the fabrication of visible-light active Cu and Ag-modified TiO_2 Nps. Our work aimed to overcome the optical imitations of titania while preserving structural integrity, maintaining biocompatibility, and boosting visible-light-induced antimicrobial activity. In this regard, a solvothermal synthetic procedure was employed for the synthesis of Cu-doped TiO_2 nano-photocatalyst and a sol-gel procedure for the decoration of TiO_2 with plasmonic Ag Nps. Corresponding bare TiO_2 Nps, from either synthetic procedure, were fabricated as a reference. The crystalline structure, phase composition, and structural properties of the unmodified and modified TiO_2 Nps were comprehensively studied by powder X-ray diffraction (pXRD). UV–vis diffuse reflectance spectroscopy (UV-DRS) was employed to investigate the optical properties of the photocatalysts, revealing their improved absorption characteristics. Raman and FT-IR spectroscopies were utilized to elucidate the molecular structures and purity, respectively. Transmission and scanning electron microscopies (TEM and SEM) were employed to examine the size and morphology of the nanomaterials. Elemental mapping and energy-dispersive X-ray spectroscopy (EDS) were applied to monitor the transition metal's content and dispersity. Prepared nanoparticles showed improved photocatalytic activity, for the degradation of the azo-dye MB, under visible light illumination. Biocompatibility was assessed on healthy human keratinocyte cell line (HaCaT) via MTT assay, while ROS production after visible light irradiation was also examined. *Escherichia coli* (*E. coli)* and *Staphylococcus aureus* (*S. aureus)* were employed as representative gram-negative and gram-positive microorganisms, respectively, to study the antibacterial effect as well as ROS generation as a potential bactericidal mechanism, after irradiation with visible light.

2. Experimental methods

2.1. Chemicals

Titanium(IV) tetraisopropoxide (97 %), Titanium(IV) butoxide (97 %) Copper(II) nitrate trihydrate – $Cu(NO_3)_2 \bullet 3H_2O$ (99 %), Tannic acid (ACS reagent grade), Anhydrous acetic acid – CH_3COOH (99.8 %),Ethanol – CH_3CH_2OH (99.8 %) and Isopropyl alcohol (IPA) (98 %) were purchased from Sigma-Aldrich and used without further purification. Sodium hydroxide beads – NaOH and Silver nitrate -$AgNO_3$ ($\geq$99 %) were purchased from Fluka. Sodium sulfate - Na_2SO_4, anhydrous (99 %) and Ethylene diamine tetraacetic acid – EDTA (99 %) were purchased from Alfa Aesar. Dulbecco's Modified Eagle Medium - DMEM, Fetal Bovine Serum -FBS, and Dulbecco's Phosphate Buffered Saline - DPBS were purchased from BioSera. Penicillin/Streptomycin and L-Glutamine for cell cultures were purchased from Sigma. 3-(4,5-dimethylthiazol-2-yl)-2,5-diphenyltetrazolium bromide - MTT was purchased from Cayman Chemical and DMSO from Sigma Life Sciences. Tryptone was provided by VWR Chemicals and Yeast extract from Condalab. High-purity double-distilled H_2O, obtained from a Rephile Milli-Q lab water system, was employed in synthesis and relevant characterization methods.

2.2. Synthesis of bare and Cu-modified TiO_2 nanoparticles

A simple solvothermal method was developed for the synthesis of bare and Cu doped TiO_2 nanoparticles. For the fabrication of TiO_2 nanoparticles with different copper dopant percentages, a solution of the titanium precursor was prepared in a round bottom flask by the dropwise addition of 1.5 ml (5 mmol) titanium tetraisopropoxide to 5 ml of absolute ethanol, under vigorous stirring, at room temperature (RT). The precursor solution was stirred for 30 min to ensure the complete dissolution of the alkoxide and it was followed by the dropwise addition of 0.6 ml (10 mmol) of anhydrous acetic acid which was used to avoid premature hydrolysis of the Ti-precursor through the coordination of the acetate ions to Ti^{4+} metal centers. In a beaker, an appropriate amount of Cu $(NO_3)_2 \bullet 3H_2O$ corresponding to 3, 5 and 10 mol% of copper/titanium precursor salts were dissolved in 5 ml of absolute ethanol and was dropwise added to the first solution. After 1 h, 1 ml of MilliQ H_2O was added dropwise and gradually the solution turned turbid indicating the nucleation and growth of amorphous Cu-doped TiO_2 particles. At this point, 0.6 ml of anhydrous acetic acid in 4 ml of absolute ethanol was injected to further retard the condensation rate. Stirring was held for 1 h after which the mixture was transferred to a stainless-steel autoclave, which was kept in a conventional oven for 8 h at 120 °C. Purification of the resulting nanoparticles was achieved through successive centrifugations with ethanol and MilliQ water to remove the unreacted precursors and the resulting pellet was dried in air at 100 °C for 8 h. Finally, highly crystalline photocatalysts were obtained after calcination at 550 °C for 2 h.

For the synthesis of bare TiO_2 nanoparticles the same procedure was followed without the addition of the copper precursor salt. The resulting photocatalysts were denoted as $_ATiO_2$, $_ATiO_2$:Cu-1, $_ATiO_2$:Cu-2, and $_ATiO_2$:Cu-3 for 0, 3, 5 and 10 mol% Cu^{2+}/Ti^{4+} respectively.

2.3. Synthesis of bare and Ag-modified TiO_2 nanoparticles

Anatase $_BTiO_2$ Nps were synthesized following a green and cost-effective sol-gel method. In a 500 ml flat bottom flask, 196.4 ml denaturated 99,9 % ethanol and 21.8 ml d d. H_2O were mixed. After 30 min of stirring, 21.8 ml (3 mmol) titanium butoxide was added dropwise (1 ml/90 s) and a white milky precipitate is formed, suggestive of TiO_2 formation. Following overnight incubation of the reaction under stirring at room temperature, the mixture was subjected to serial centrifugations (twice with ethanol, twice with d.d. H_2O, and once more with ethanol) at 6000 rpm to purify the final product. The precipitate was collected and dried overnight in an

incubator at 80 °C, followed by annealing for 2 h at 500 °C. The white powder of $_B$TiO$_2$ Nps was collected and stored at ambient temperature. This reaction yielded approximately 5.22 g.

Ag Nps were synthesized through a simple, green, and cost-effective one-pot reaction. Briefly, 20 mg of Tanic Acid (TA) and 2 mg of NaOH are dissolved in 500 μl of double distilled (d.d.) H$_2$O.The yellow solution is then mixed with 9 ml of denaturated 99,9 % ethanol, promoting a green-colored dispersion, after 10 min of stirring. An aqueous solution of AgNO$_3$ (10 mg in 500 μL) is added dropwise and an instant color change to deep brown is noticed, indicating the formation of Ag Nps. Following another 10 min, the reaction mixture is centrifuged at 14000 rpm for 2 min, to remove byproducts and unreacted materials. Ag Nps were purified following redispersion in d.d. H$_2$O and another centrifugation at 14.000 rpm for 15 min. The final precipitate was collected and redispersed in 2 ml d d. H$_2$O with a final measured concentration of 1.97 mg/ml.

The synthetic procedure of AgNps was carried out in the same ethanolic solution used for the production of $_B$TiO$_2$, as a proof of concept for the subsequent one-pot reaction of AgNps' incorporation on $_B$TiO$_2$. Thus, the synthesis of hybrid $_B$TiO$_2$:Ag Nps was conceptualized by merging the previously followed synthetic procedures of distinct Ag Nps and $_B$TiO$_2$ Nps. The concept entails the concurrent formation of nanoparticulate $_B$TiO$_2$ and Ag. This is realized by first dispersing, in the following order, i) NaOH, ii) TA, and iii) 1 ml titanium butoxide (3 mmol) in 9 ml denaturated 99,9 % ethanol, under stirring. After 10 min, 1 ml aqueous solution of AgNO$_3$, at different concentrations, is added dropwise, acting at the same time as an initiator of the sol-gel reaction for the formation of $_B$TiO$_2$ and as a source of Ag $^+$ ions to be reduced by TA, in an alkaline environment, forming Ag Nps. To try various percentages of $_B$TiO$_2$ decoration with Ag Nps, different amounts of reactants were used: $_B$TiO$_2$:Ag-1 Nps: 2 mg NaOH, 20 mg TA and 10 mg AgNO$_3$ (Ag: 4.5% Wt, 2%mmol$_{Ag/Ti}$), $_B$TiO$_2$:Ag-2 Nps: 20 mg NaOH, 100 mg TA and 15 mg AgNO$_3$ (Ag: 6.8%Wt, 3%mmol$_{Ag/Ti}$), $_B$TiO$_2$:Ag-3 Nps: 20 mg NaOH, 100 mg TA and 50 mg AgNO$_3$ (Ag: 22.6%Wt, 3%mmol$_{Ag/Ti}$).

2.4. Structural analysis methods and techniques

Powder X-ray diffraction (pXRD) patterns of the synthesized samples were recorded with a Bruker D8 Advance diffractometer in Bragg-Brentano geometry, operating at 40 kV of voltage and 25 mA of current. The X-ray source was a Cu anode with a Cu-Ka$_1$ (λ = 1.5418 Å) radiation. The use of a Göbel mirror made any interferences from Cu-Ka$_2$ negligible. The diffraction patterns were recorded at a 2θ° range of 15–80° with a 0.04°/s step size and 1.6s/step scan speed.

Crystallite size (D) was calculated using the Scherrer equation:

$$D = \frac{K\lambda}{\beta \cos \theta} \tag{1}$$

where K represents the shape factor (0.89 in this case), λ corresponds to the X-ray wavelength, β denotes the full width at half maximum (FWHM) of the diffraction peak arising from the (101) hkl plane and θ represents the Bragg angle.

Raman spectra were collected with a Micro-Raman Renishaw inVia Qontor spectrometer equipped with a 532 nm argon laser.

Absorption and Diffusion Reflectance spectra were collected in a UV–Vis Spectrophotometer with an integrating sphere attachment (UV-2600i & ISR-2600Plus, SHIMADZU). Samples were prepared by uniformly dispersing each nanostructure in the form of a dried powder at 1 % in barium sulfate (BaSO$_4$), forming a pellet of the photocatalysts. Pure BaSO$_4$ served as a reference. The data collected were transformed to Kubelka-Munk plots by plotting ((F(R$_\lozenge$)hv)$^{1/2}$ versus the excitation energy hv, for the calculation of the indirect bandgap of TiO$_2$. The exact value of the bandgap energy was found by extending the linear fit of the steepest part in the curve below 390 nm, to the point of zero photon energy (E = 0). Urbach energy calculations were carried out by plotting lnα versus the photon energy (E). The Urbach energy value was calculated by the reciprocal of the slope of the linear portion below the optical bandgap of TiO$_2$, via the following equation:

$$a = a_0 \exp \left(\frac{E}{E_u} \right) \tag{2}$$

where α is the absorption coefficient, E is the photon energy and E$_u$ is the Urbach energy. The calculation of the Urbach energy for each case was performed by plotting ln(α) vs E and the reciprocal of the slope of the linear part below the bandgap resulted in the Urbach energy value in eV.

Fourier Transform Infrared (FT-IR) spectra of powdered samples were acquired with a Shimadzu IRAffinity-1/IRsolution spectrometer, equipped with an attenuated total reflectance (ATR) diamond-based accessory.

XPS measurements were carried out in an ultra-high vacuum (UHV) chamber at a working pressure of 5•10^{-10} mbar, using a non-monochromatic AlKa radiation line (1486.6 eV) and an electron energy analyzer (Leybold LH EA11) operated at 100 eV pass energy. Samples were prepared by pressing the catalyst powder on a thin lead sheet. The under-analysis area was a 4•5 mm^2 rectangle and quoted binding energies are accurate to 0.1 eV. All spectra were charge corrected with reference to adventitious carbon at 284.8 eV, while surface atomic ratios were calculated using proper experimental relative sensitivity factors.

2.5. Colloidal stability

Hydrodynamic diameter (d$_{DLS}$) and the zeta potential (ζ) were recorded in aqueous suspensions of the samples at 1 mg/ml by dynamic light scattering (DLS, Malvern Instruments Ltd, Nano-ZS, He–Ne laser 633 nm). The plots of size distribution by %Number intensity and ζ-potential distribution by Total counts are presented as averaged distribution values from three consecutive (10 s time

interval) measurements of 10 and 20 runs, respectively.

2.6. Morphology assessment via electron microscopy

Morphological characterization was carried out by scanning electron microscopy (SEM, Inspect Microscope, FEI, 15–25 keV) and transmission electron microscopy (TEM, FEI Talos F200i field-emission (scanning) transmission electron microscope - Thermo Fisher Scientific Inc., Waltham, MA, USA-operating at 200 kV, equipped with a windowless energy-dispersive spectroscopy microanalyzer - 6T/100 Bruker, Hamburg, Germany). SEM samples of dried powders were prepared on conductive carbon tape and coated with a thin layer of gold under *in vacuo*. TEM samples of ethanolic suspensions were drop-casted on suitable grids (copper grid for $_B$TiO$_2$, Ag, and $_B$TiO$_2$:Ag-1 *vs* nickel grid for $_A$TiO$_2$, and $_A$TiO$_2$:Cu-1). Size distributions, of the studied nanostructures derived from SEM (d_{SEM}) and TEM (d_{TEM}) images, were calculated after measuring the diameter of individual distinct nanoparticles (40–100) via the ImageJ software.

2.7. Photodegradation of MB

The degradation of the model azo dye MB was studied, to evaluate the photocatalytic responsiveness of Cu-doped and Ag-decorated TiO$_2$ Nps to visible light. Each sample was dispersed in d.d. H$_2$O at 0.25 mg/ml in a glass vial and sonicated for 15 min, to ensure uniform dispersion of the nanocatalyst. Then, MB was added in each vial at a final concentration of 15 μM, which was placed under magnetic stirring at 500 rpm in the dark for 30 min, to measure the adsorbed amount of the dye on the photocatalyst's surface. The samples were then irradiated over the course of 300 min under visible light irradiation (2xVT 4922 visible-light LED lamps at 20 mV, 10 cm distance), at 25 °C. Degradation measurements were executed every 60 min. For each measurement, 2 ml of each sample was centrifuged at 10000 rpm and the supernatant's absorption spectra were measured with a double-beam Shimadzu UV1900 UV–Vis Spectrometer (Shimadzu, Hesse, Germany) operating at 25 °C. The pellet was then redispersed in the collected supernatant and returned to the reactor, to maintain the initial concentration balance of the reactants.

The photodegradation efficacy of the nanocatalysts was assessed via calculations of the dye degradation percentage (D%), the pseudo-first-order kinetics (k_{deg}), and the half-life time of MB ($t_{1/2}$). The mathematical formulas that were used are listed below:

$$D\% = (C_t / C_0) \times 100 \tag{3}$$

$$\ln (C_t / C_0) = -k_{deg} \times t \tag{4}$$

$$t_{1/2} = (0.693 / k_{deg}) \tag{5}$$

where D% is the degradation percentage, C_0 is the initial MB concentration, C_t is the MB concentration at each time interval, k_{deg} is the degradation rate constant and $t_{1/2}$ is the half-life period. In order to identify the active species generated upon visible light absorption that contribute to the degradation of MB, radical scavenging experiments were conducted. The scavengers chosen were IPA, as a hydroxyl radical scavenger, EDTA as a hole scavenger and Na$_2$SO$_4$ as an electron scavenger [71,72]. The experimental procedure followed was the same as that described previously, except that appropriate amounts of each scavenger were added to reach a final concentration of 4 mM, after reaching the adsorption-desorption equilibria of MB on the catalysts.

2.8. Cell culture

Immortalized cultured human keratinocyte cell line (HaCaT) was employed as a model healthy cell line to assess the biocompatibility of the herein synthesized nanostructured materials. HaCaT cells were cultured in DMEM supplemented with 10 % v/v heat-inactivated FBS, 2 mM L-glutamine, and antibiotics (100 units/mL penicillin and 100 μg/mL streptomycin) at 37 °C in a 5 % CO$_2$ atmosphere.

For the MTT and ROS assays, cells were dissociated from a fully confluent HaCaT monolayer cell culture following a 10 min exposure to 1.5 ml of Trypsin and subsequently gathered in sterile falcon tubes, filled with 5 ml of fresh culture medium. The cellular suspension underwent centrifugation at 480g, after which the resulting cell pellet was resuspended in fresh medium at a concentration tailored to the specific assay requirements.

2.9. Cellular viability – MTT assay

In a 96-well plate, 100 μl from a suspension of 0.01*10^6 cells/ml in culture medium was aliquoted in each well and incubated at 37 °C, under 5 % CO$_2$, for 24 h to reach approximately 70 % confluency. Subsequently, the supernatant was aspirated and serial suspensions of the examined nanomaterials (1, 5, 10, 25, 50, and 100 μg/ml) were inserted in triplicate wells, for each concentration, while triplicates of pure culture medium served as control samples. Following another 24 h incubation, treated control samples were extracted, washed with PBS, treated with 100 μl of MTT (yellow solution of 3-(4,5-dimethylthiazol-2-yl)-2,5-diphenyl-2H-tetrazolium bromide in PBS, 1 mg/ml), during which MTT underwent enzymatic reduction, resulting in the formation of purple formazan crystals. After 4 h incubation, the MTT solution was removed, and the crystals were diluted with 100 μl DMSO. Using an ELISA plate reader (Sirio S, SEAC Radim group), the absorbance of each well was recorded at 540 nm, with a reference wavelength set at 620 nm. The

concentration variability of the formazan crystals, a product of the MTT treatment, was directly proportional to cellular viability, which is determined by the equation [73]:

$$\% \ Cell \ Viability = \frac{A_{sample}}{A_{control}} * 100 \qquad (6)$$

where A_{sample} and $A_{control}$ represent the average absorbance values for each sample and the control, respectively.

The same protocol was implemented after the ROS assay to assess cellular viability after light irradiation.

2.10. Cellular spectrofluorimetric and microscopic ROS detection

In a 96-well plate, 100 μl from a suspension of $0.15*10^6$ HaCaT cells/ml in culture medium was aliquoted in each well and incubated at 37 °C, under 5 % CO_2. After 24 h incubation, when the cellular monolayer had reached confluency, the medium was aspirated and replaced with 100 μl suspensions of the examined nanomaterials in cultured medium without FBS, at a concentration of 50 μg/ml in triplicates. 100 μl of pure culture medium without FBS and 200 μM H_2O_2, were also added in triplicate, which served as negative and positive controls. The plates were prepared in duplicates and incubated for 3 h 40 min in the dark. Afterward, for 20 min, one plate was left in the dark and the other was subjected to visible light irradiation at 37 °C. the medium was then removed from each well and replaced by 100 μl of freshly prepared 10 μM the cell-permeant nonfluorescent 2′,7′-dichlorodihydrofluorescein diacetate (H_2DCFDA) which serves as a fluorescent indicator of intracellular ROS production, after acetate group cleavage to the fluorescent molecule of DCF by intracellular esterase and oxidation [74,75]. After 30 min incubation at 37 °C, each well was washed with PBS and the resulting fluorescence intensity was recorded in a microplate reader (Infinite 200, TECAN i-Control) with excitation and emission wavelengths at 485 nm and 535 nm, respectively. The graphs were plotted as the relative fluorescence intensity according to the equation:

$$\% \ Relative \ Fluorescence \ Intensity = \frac{F_{sample}}{F_{negative \ control}} * 100 \qquad (7)$$

Where F_{sample} and $F_{negative \ control}$ represent the mean fluorescent intensity of the cells treated with each sample and negative control, respectively.

To visualize ROS production microscopically, 500 μl of $0.1*10^6$ HaCaT cells/ml were seeded in a 24-well plate containing glass coverslips and incubated for 24 h at 37 °C, under 5 % CO_2. Then, each well was cleared by the medium, washed with PBS, and filled with 50 μg/ml suspensions of the samples in culture media without FBS. The following procedure included the same steps as the spectrofluorimetric ROS assay to cross-validate the results optically. Thus, after the 30 min incubation with H2DCFDA, the samples were washed with PBS and placed on glass slides. Observation of the biological samples was conducted through widefield optical microscopy (EXI-310, AccuScope Inc. & Unitron) and fluorescence microscopy (OMAX Trinocular Compound EPI-Fluorescence Microscope M834FLR with 1.3 MP CMOS Camera (Blue filters: Excitation 410–490 nm, Emission: 515 nm and Green filters: Excitation 490–540 nm, Emission: 590 nm).

2.11. Microbial cultures

Escherichia coli (*E. coli*) and *Staphylococcus aureus* (*S. aureus*) were employed as model gram-negative and gram-positive bacterial strains, respectively. Bacteria were grown in Lauria Broth (LB) at 37 °C with 250 rpm agitation. After 24 h, bacterial cultures were subjected to centrifugation at 3000 rpm for 3 min and the collected bacteria were redispersed in PBS. The optical density at 600 nm (OD_{600}) of the stock bacterial cultures was determined via a spectrophotometer. Bacterial inoculums were adjusted to $OD_{600} = 0.15$ for further evaluation.

2.12. Antimicrobial activity and ROS detection

In a sterile 24-well plate, 1 ml of *E. coli* or *S. aureus* inoculums containing the modified or unmodified titania nanostructures (1 mg/ml), $Cu(NO_3)_2.3H_2O$ (1 mg/ml) and Ag Nps (30 μg/ml) were placed in each well. Control samples (negative control) of untreated inoculums and treated (positive control) with H_2O_2 and moxifloxacin (5 μg/ml) were also included. Each plate of either bacterial strain was prepared in duplicate and incubated in dark or under visible light irradiation at 37 °C for 24 h. Following, the samples were separately aspirated from each well, centrifuged at 3000 rpm for 3 min, and redispersed in 1 ml PBS.

To evaluate the antimicrobial activity, 100 μl of each sample was aliquoted in a 96-well plate and the OD_{600} was recorded in an ELIZA plate reader. To assess the potential of ROS production as an antibacterial mechanism of the tested nanostructures, the H2DCFDA method was applied again as a routine protocol for bacterial cultures as well [76,77]. Briefly, 100 μl of H2DCFDA was added in each well at a final concentration of 10 μM. After 30 min incubation at 37 °C the fluorescent signal was recorded in a microplate reader (Infinite 200, TECAN i-Control) with excitation and emission wavelengths at 485 nm and 535 nm, respectively. The collected data were expressed as % Relative Fluorescence Intensity according to equation (7).

Similarly, 250 μl of each sample was transferred in Eppendorf tubes, mixed with H2DCFDA at a final concentration of 10 μM, and incubated in the dark for 30 min at 37 °C. Finally, 10 μl of each sample was placed on a glass slide, covered with a coverslip, and observed via fluorescent microscopy.

2.13. Statistical analysis

Biocompatibility and antimicrobial assessment results were subjected to two-way ANOVA statistical analysis, with 95 % confidence interval, by implementing Tukey's or Šídák's multiple comparisons tests, respectively. The analyses were performed with GraphPad Prism by applying the GraphPad (GP) method with significance expressed as: ****($p \leq 0.0001$), *** ($p \leq 0.001$), **($p \leq 0.01$), * ($p \leq 0.05$). Non-significant results, with $p > 0.05$, are not assigned in the graphs.

3. Results and discussion

3.1. Structural characterization

According to the pXRD diffraction patterns of bare TiO_2, Cu, and Ag-modified TiO_2 Nps (Fig. 1), changes in crystallite size, lattice parameters, and microstrain were monitored for each sample obtained through the two distinct synthetic procedures. The diffraction peaks at 25.3°, 36.9°, 37.8°, 38.6°, 48°, 53.9°, 55.1°, 62.1°, 62.7°, 68.8°, 70.3°, 74.1°, 75.1° and 76° corresponding to the (101), (103), (004), (112), (200), (105), (211), (204), (116), (220), (215), (301) planes of tetragonal anatase TiO_2 can be well indexed to the COD:5000223 entry card for both $_ATiO_2$ and $_BTiO_2$. No additional phases ascribed to the dopant, such as metallic copper or copper oxides can be detected in Cu-doped $_ATiO_2$ samples, even at high dopant percentages (Fig. 1 A). The absence of rutile suggests that the crystal phase remains unaltered upon doping and the most catalytically active phase of anatase is retained. For bare titania nanoparticles obtained through the sol-gel procedure, $_BTiO_2$ Nps, a minor percentage (1 %) of the meta-stable crystal phase of brookite (COD:9004141) was detected, possibly originating from synthetic parameters like the use of room temperature.

It is noteworthy that the existence of brookite is unverified in the Ag-modified samples due to the co-existence of the amorphous part of the Ag modifier, seemingly appearing at the same 2θ° as the strongest diffraction peak of orthorhombic brookite, ascribed to the (211) plane. Additionally, with the increase of Ag content in $_BTiO_2$:Ag-2 and $_BTiO_2$:Ag-3 Nps, the appearance of diffraction peaks at the (111), (200), (220), and (311) crystal planes of FCC metallic Ag (COD:1100136), were noticed. This indicates the crystallization and growth of Ag clusters on the surface of $_BTiO_2$ grains, leading to surface modification, rather than incorporation into the titania's crystal lattice [78]. Broad peaks are observed in all samples due to the presence of crystallites in the nanometre range.

The well-defined diffraction peaks in the $_ATiO_2$:Cu series suggest the isotropic growth of the crystallites. Rietveld refinement and fitting of the (101) planes (Table S1) at every sample revealed a slight increase in the crystallite size of $_ATiO_2$ (d_{XRD}: 18.5 nm) upon doping with 3mol%Cu (d_{XRD}: 19.5 nm) and 5mol%Cu (d_{XRD}: 21 nm), followed by a decrease for 10mol%Cu (d_{XRD}:19.5 nm). This trend could be attributed to the incorporation of Cu^{2+} dopant in the spaces between atoms of the TiO_2 lattice, which facilitated the formation of stable nucleation sites during the crystallization process for the growth of larger crystallites.

Substitutional doping of Cu^{2+} ions (0.73 Å) into positions previously occupied by Ti^{4+} ions (0.605 Å) could be implied by the increase of the lattice constants and the anatase cell volume expansion [79,80] (Table S1). Additionally, the existence of Cu^{2+} ions in solution could have altered the energy barrier for crystal growth favoring the growth of larger crystallites, while preventing the agglomeration of smaller ones.

These effects ceased to exist when the concentration of Cu increased ($_ATiO_2$:Cu-3). A possible explanation could be that the excess Cu^{2+} ions act as nucleation sites for the growth of CuO clusters, rather than effectively doping the anatase lattice by substituting significantly larger numbers of Ti^{4+} ions when compared to $_ATiO_2$:Cu-2. It is important to note that the absence of CuO diffraction peaks suggests the small fraction of such clusters or the presence of amorphous $Cu(OH)_2$.
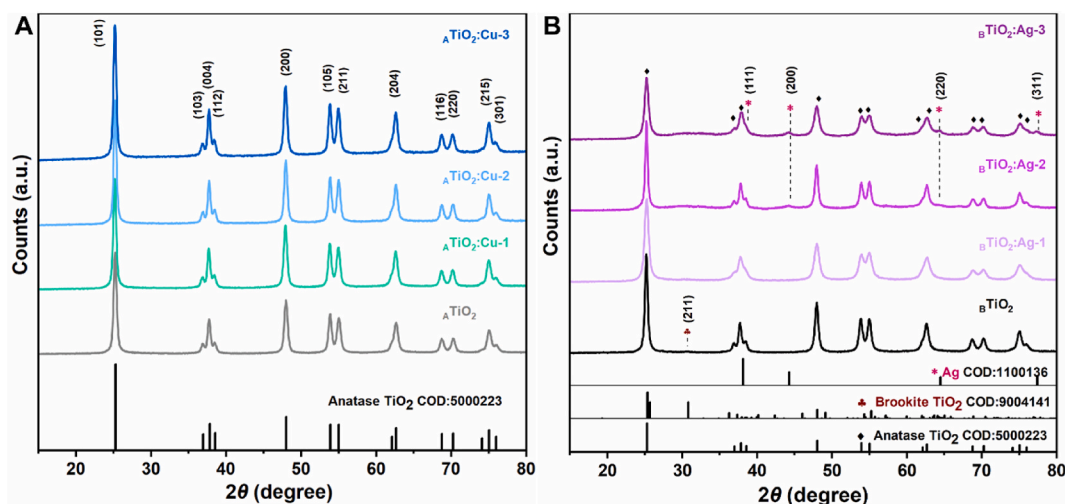
Fig. 1. Powder diffraction patterns of (A); $_ATiO_2$, $_ATiO_2$:Cu-1, $_ATiO_2$:Cu-2, $_ATiO_2$:Cu-3 and (B); $_BTiO_2$, $_BTiO_2$:Ag-1, $_BTiO_2$:Ag-2, $_BTiO_2$:Ag-3, in comparison with the corresponding Crystallography Open Database (COD) patterns for anatase, brookite and silver.

The crystallite size of the Ag-modified $_B$TiO$_2$ Nps obtained through the sol-gel synthetic procedure exhibits different dynamics. The introduction of Ag leads to a drastic decrease in the crystallite size of $_B$TiO$_2$:Ag-1 (d_{XRD}:15.2 nm). This result could indicate substitutional doping of $_B$TiO$_2$'s anatase lattice leading to the microstrain increase of the crystal lattice and shrinkage of the crystallites due to the different ionic radius of Ag$^+$ ions (1.26 Å), when compared to Ti^{4+} ions (0.68 Å), in the coordination state [81]. This is confirmed by Rietveld Refinement data (Table S1), as the microstrain value of $_B$TiO$_2$:Ag-1 appears augmented, compared to bare $_B$TiO$_2$. It is worth mentioning here that plain Ag Nps exhibited a d_{XRD} equal to 5.7 ± 0.2 nm (Table S1) further supporting that the existence of nanosilver on $_B$TiO$_2$ could result in an apparent increase in the crystallite size. At higher fractions of Ag modifier, the effect of the Ag$^+$ ions on TiO$_2$ changed and led to an increase of the crystallite in $_B$TiO$_2$:Ag-2 (d_{XRD}:26 nm), while the microstrain (%) was maintained at the same level as $_B$TiO$_2$, indicating separate Ag cluster-growth from $_B$TiO$_2$, impacting only the growth of the crystallites by functioning as nucleation sites. The excess of Ag in $_B$TiO$_2$:Ag-3 (d_{XRD}:16.2 nm) inhibited the growth of anatase crystallite and reduced the crystallinity.

The Raman spectra (Fig. 2 B, E) of all samples correspond to the anatase phase with no other modes pointing to other inorganic crystalline structures. For the unmodified $_A$TiO$_2$ and $_B$TiO$_2$ intense modes at 144 cm^{-1} and two less intense modes at 197 and 637 cm^{-1} correspond to the E$_g$ mode of anatase while the modes at 396 cm^{-1} and 515 cm^{-1} correspond to B$_{1g}$ and A$_{1g}$ + B$_{1g}$ modes. The E$_{1g}$ mode of TiO$_2$ is related to the (101) direction of the crystal and the symmetric bending vibration of O–Ti–O along the c-axis [82,83]. Substitution of Ti^{4+} ions from different ions can impact the position of the E$_{g1}$ mode. This effect is assigned to the different ionic radii of dopant ions, herein Cu^{2+} and Ag$^+$. In the case of Cu-doped TiO$_2$, a blueshift is observed in the position of the E$_{1g}$ mode, indicating the substitution of Ti^{4+} from Cu^{2+} and the formation of oxygen vacancies for charge compensation, in the $_A$TiO$_2$ lattice [83–85]. For $_B$TiO$_2$: Ag-1 a similar blueshift to higher wavenumbers is noticed suggesting lattice distortion by oxygen vacancies' creation through the incorporation of Ag$^+$, in a similar manner. In $_B$TiO$_2$:Ag-2 no blueshift, as compared to bare $_B$TiO$_2$, is observed, confirming the XRD results. Interestingly, at the highest concentration of Ag, an important blue shift of E$_{g1}$ paired with a noticeable peak broadening could be indicative of Ag$^+$ interaction with oxygen ions on the surface of $_B$TiO$_2$ and of phonon confinement effects generated by $_B$TiO$_2$'s lattice defects.

IR-ATR spectra of the nanostructures (Fig. 2C–F) depict the purity and the characteristic bond vibrations of each sample's constituents. All samples exhibit a broad vibration in the range of 500–912 cm^{-1} which is ascribed to the typical stretching vibration of Ti - O – Ti bonds in the crystal lattice of anatase [86]. Vibration at 1637 cm^{-1}, observed in all samples, is attributed to –OH groups from either Ti–OH bending vibrations or to adsorbed H$_2$O molecules. The broad bands at 3000–3300 cm^{-1} arise from the stretching vibrations of the surface adsorbed –OH groups [87,88]. By increasing the amount of Cu or Ag modifiers in both cases, these vibrations become weaker, indicating their presence on the surface of TiO$_2$ Nps, binding to Ti^{4+} sites.

Further confirmation of successful Ag embedment comes from the rise of another band at 1360 cm^{-1}, assigned to Ag - O – Ti bond formation, which sharpens as the Ag content increases (Fig. 2 F). A weak vibration at 2340 cm^{-1} of the bare and Cu-modified nanoparticles can be attributed to –CO$_2$ surface adsorbed moieties (Fig. 2C) [89–92].

XPS measurements were conducted on bare $_A$TiO$_2$ and $_B$TiO$_2$ as well as on selected photocatalysts $_A$TiO$_2$:Cu-1, $_A$TiO$_2$:Cu-3 and $_B$TiO$_2$:Ag-2, $_B$TiO$_2$:Ag-3 in order to identify the oxidation states of the surface components. Fig. 3 (a) shows the XP spectra of the Ti 2p
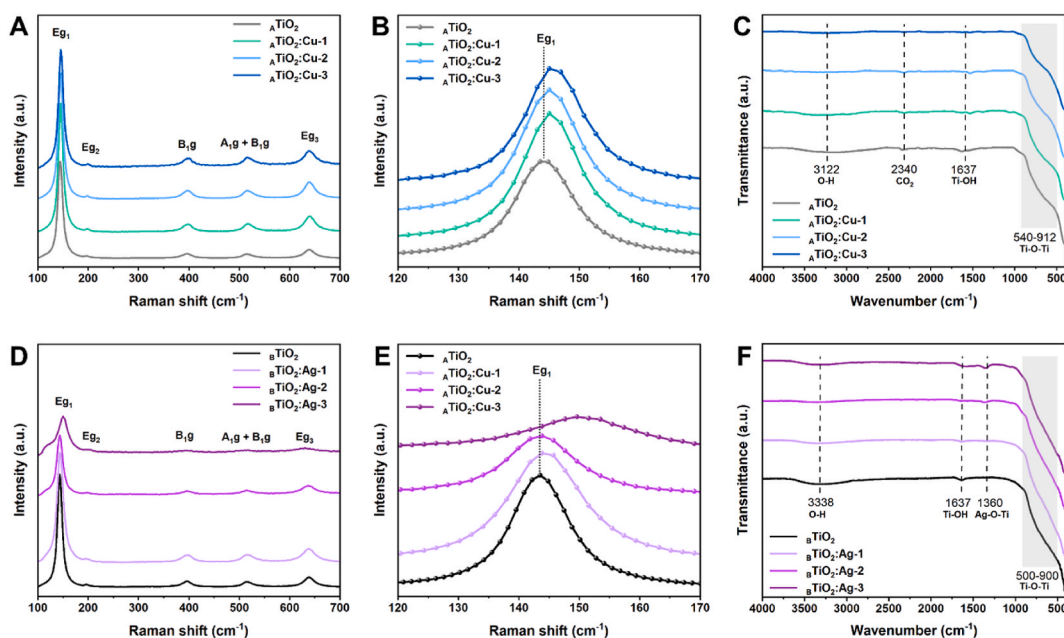

Fig. 2. (A, D) Raman active modes of $_A$TiO$_2$(:Cu-1, 2, 3) and $_B$TiO$_2$(:Ag-1, 2, 3) (B, E); Shifting of the E$_{g1}$ mode at 144 cm^{-1} (C, F) IR-ATR spectra of the samples.
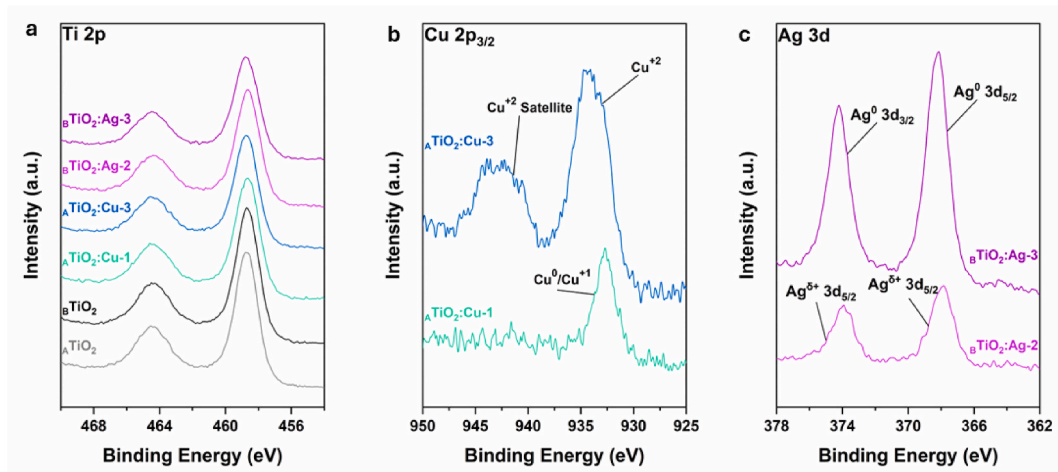
Fig. 3. High resolution XPS spectra of the selected catalysts depicting (a) Ti2p, (b) Cu $2p_{3/2}$ and (c) Ag 3d

region. The two peaks correspond to the $2p_{3/2}$ and $2p_{1/2}$ doublet at 458.7 and 464.3 eV, characteristic values for Ti^{4+} [93]. The Ti 2p peak in combination with the O 1s peak (Supporting information) show no clear signs of defect formation, which in the case of the Ti 2p spectra would appear as a shoulder for the $2p_{3/2}$ line at 457.3 (Ti^{3+}).

The Cu $2p_{3/2}$ spectra (Fig. 3 B) for sample $_ATiO_2$:Cu-1 shows a main feature centered at 932.6 eV, which may be attributed to either metallic (Cu^0) or oxidized (Cu^{+1}) copper. Distinguishing between these two oxidation states is typically performed utilizing the modified Auger parameter calculated from the Cu Auger LMM peaks and main photoelectron Cu$2p_{3/2}$ line [94]. However, in the present case the Cu LMM peaks overlap with the region of the Ti 2s peak. Taking into account that the Ti is in vast excess in the sample, the signal for the Cu LMM peaks cannot yield any meaningful information. It should be noted that the complete absence of any satellite peaks at the high binding energy side of the main Cu $2p_{3/2}$ line suggests that most likely the Cu is in the metallic (Cu^0) state in this sample. In the case of the $_ATiO_2$:Cu-3 sample, the $2p_{3/2}$ peak shows an increase in width combined with a shift to higher binding energies (933.9 eV). This observation together with the presence of a large satellite peak at 942.6 eV confirms that the copper in this sample is in the Cu^{+2} oxidation state [93,95,96].

The Ag 3d spectra can be observed in Fig. 3C. For the $_BTiO_2$:Ag-3 sample the $3d_{5/2}$ and $3d_{3/2}$ peaks center at 368.2 and 374.2 eV respectively, which are characteristic for Ag in the metallic state. A negative shift of about -0.3 eV is observed for the Ag 3d spectrum for the $_BTiO_2$:Ag-2 sample, suggesting most likely the presence of silver at a higher oxidation state ($Ag^{\delta+}$). Note that the consensus regarding Ag 3d is that increased oxidation state leads to a negative shift in binding energies, supporting the above claim for silver oxide formation (Ag_2O or AgO) [97,98]. Taking also into account the pXRD measurements, where the only observable phase attributed to Ag species is metallic Ag, the small negative shift of the Ag 3d peaks can be attributed to the development of an oxide layer covering part of the metal nanoparticle surface. Survey scans of the samples and C 1s and O 1s high resolution scans can be found in the supplementary material (Fig. S1). Note the presence of the Pb 4d peak is due to the thin sheet used to deposit the sample for analysis. Moreover, samples $_BTiO_2$:Ag-2 and $_BTiO_2$:Ag-3 show amounts of sodium present. This is attributed to the preparation methods used in our study.

3.2. Morphology and colloidal stability

According to both TEM (Fig. 4 & Fig. S2a) and SEM (Fig. 5 and Fig. S2b) analysis, the synthetic route for $_ATiO_2$ Nps (d_{SEM} = 19,8 nm, d_{TEM} = 20,2 nm) resulted in smaller-sized nanoparticles, than the method employed to produce $_BTiO_2$ Nps (d_{SEM} = 89,4 nm, d_{TEM} = 82,1 nm). It is noteworthy that $_BTiO_2$ Nps in SEM appear as spherically formed nanostructures, but a cluster-like form is revealed in TEM images. Each cluster consists of smaller and irregularly shaped nanostructures around 16 nm, which could be correlated with the apparently smaller d_{XRD} (Table 1). In the case of Cu-modified $_ATiO_2$ Nps, size distribution (Fig. S3) remains around 20 nm, as Cu is incorporated in the structure in the form of ions. Ag-modified $_BTiO_2$ Nps demonstrated slight size expansion (Fig. 5 & Fig. S3) since Ag is deposited in the form of polycrystalline nanoparticles around 8 nm, which is in accordance with the size distribution of pure Ag Nps (Fig. S3). This structural and morphological difference between the samples is attested by the elemental mapping performed on $_ATiO_2$:Cu-1 Nps (Fig. 4C1-C6) and $_BTiO_2$:Ag-1 Nps (Fig. 4 D1-D6), where Cu is observed scattered in the entirety of the sample, whereas Ag is observed as defined spots within the structure.

EDS analysis from SEM (Fig. 5C and D) verified the effective Cu or Ag incorporation, as well as the increasing metal content in the structure of titania, approximating the initial concentration of each metal during either synthetic approach. For the selected samples of $_ATiO_2$:Cu-1 Nps and $_BTiO_2$:Ag-1 Nps, the mass fraction (%Wt) of each metal is 2.77%Wt$_{Cu}$ and 3.33 %Wt$_{Ag}$, respectively, which is consistent with the corresponding EDS analysis from TEM (2.35%Wt$_{Cu}$ and 3.19 %Wt$_{Ag}$) (Fig. S4). Additionally, from the Selected Area Electron Diffraction (SAED) analysis performed via HR-TEM (Fig. S5) -as a supplementary analysis of the Nps' crystal structure to XRD-
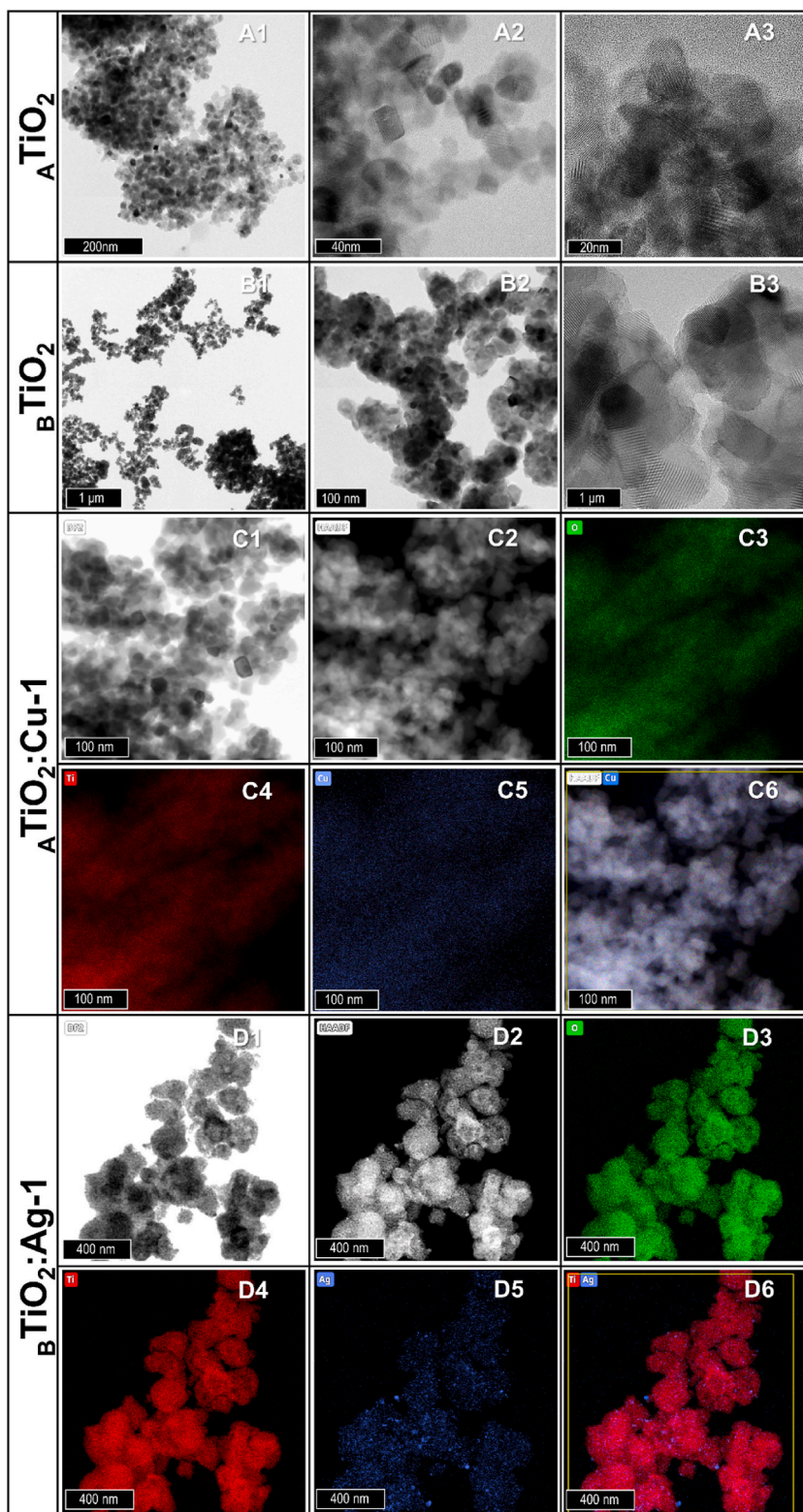
Fig. 4. TEM images of (A1-3) $_A$TiO$_2$ Nps, B1-3) $_B$TiO$_2$ Nps, (C1-6) $_A$TiO$_2$:Cu-1 with elemental mapping, (D1-6) $_B$TiO$_2$:Ag-1 with elemental mapping.
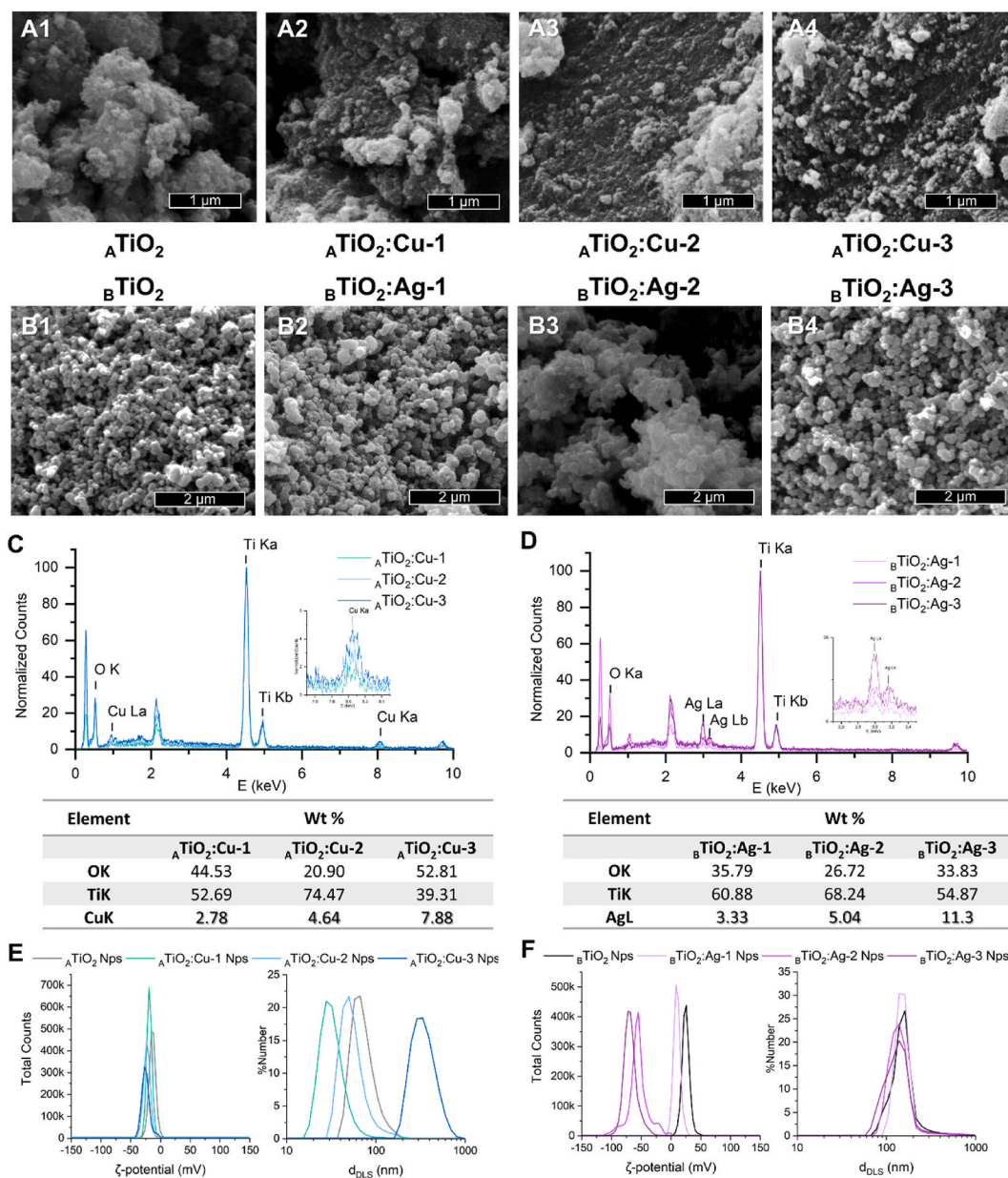
Fig. 5. (A1-4) SEM images of $_A$TiO$_2$ and $_A$TiO$_2$:Cu-1 to 3. (B1-4) SEM images of $_B$TiO$_2$ and $_B$TiO$_2$:Ag-1 to 3. EDS analysis and Wt% elemental quantification of © $_A$TiO$_2$:Cu-1 to 3 and D) $_B$TiO$_2$:Ag-1 to 3. Hydrodynamic radius (d$_{D:S}$) and ζ-potential distribution of (E) $_A$TiO$_2$ and $_A$TiO$_2$:Cu-1 to 3, and (F) $_B$TiO$_2$ and $_B$TiO$_2$:Ag-1 to 3.

the crystal lattice of anatase is verified for both $_A$TiO$_2$ and $_B$TiO$_2$ Nps, which is also maintained in the corresponding modified samples of $_A$TiO$_2$:Cu-1 Nps and $_B$TiO$_2$:Ag-1 Nps. For $_B$TiO$_2$:Ag-1 the d-spacing of the (111) hkl assigned to Ag^0 nanoparticles is observable and indicates the existence of Ag^0 nanoparticles on the surface of $_B$TiO$_2$. Morphological and elemental analysis revealed a successful approach towards our synthetic intention, considering that the aim of both synthetic procedures was to incorporate Cu as a dopant ion and Ag in the form of embedded plasmonic nanoparticles.

The colloidal stability of all the samples was tested in aqueous dispersions at room temperature. The hydrodynamic diameter (d$_{DLS}$) of all samples (Fig. 5 and Table 1) is slightly increased compared to d$_{TEM}$ and d$_{SEM}$, which is expected as there are several molecular dynamics at play among nanoparticles and water molecules. It is noteworthy that smaller-sized $_A$TiO$_2$ Nps demonstrated a slightly negative ζ potential of −13.2 mV, whereas larger cluster-like $_B$TiO$_2$ exhibited a moderately positive one around +25.3 mV (Fig. 5E–D). Morphological discrepancies as well as synthetic differences have often been reported to affect the ζ potential trend of TiO$_2$, either due to size and shape anisotropies, or variations in synthetic parameters like Ti source and other additives [99–101].

In the case of $_A$TiO$_2$:Cu Nps, as the amount of Cu increases, the ζ potential slightly shifts towards more negative values reaching

Table 1

Comparative data of unmodified and modified titania nanostructures of the crystallite size (d_{XRD}), nanoparticle diameter calculated from TEM (d_{TEM}) or SEM (d_{SEM}), and of DLS rendered hydrodynamic diameter (d_{DLS}), Polydispersity index (PdI) and ζ-potential.

Sample	d_{XRD} (nm)	d_{TEM} (nm)	d_{SEM} (nm)	d_{DLS} (nm)	PdI	ζ (mV)	Sample	d_{XRD} (nm)	d_{TEM} (nm)	d_{SEM} (nm)	d_{DLS} (nm)	PdI	ζ (mV)
$_A$TiO$_2$	18,465	20,2 ± 5,7	19,81 ± 4,55	74,47 ± 23,9	0,266	13,2 ± 5,4	$_B$TiO$_2$	21,697	82,1 ± 18,2	89,4 ± 13,3	165,1 ± 96,76	0,370	25,3 ± 6,38
$_A$TiO$_2$: Cu-1	19,544	21,9 ± 5,4	23,93 ± 6,2	33,55 ± 11,4	0,466	18,4 ± 4,24	$_B$TiO$_2$: Ag-1	15,222	140,4 ± 37,0	127,1 ± 44,2	167,3 ± 30,1	0,518	10,4 ± 5,73
$_A$TiO$_2$: Cu-2	20,891	–	22,20 ± 5,52	57,41 ± 24,27	0,477	22,8 ± 5,31	$_B$TiO$_2$: Ag-2	26,354	–	131,4 ± 24,0	154,3 ± 94,4	0,387	54,9 ± 13,6
$_A$TiO$_2$: Cu-3	19,506	–	22,05 ± 4,85	357,9 ± 109,9	0,534	24,8 ± 6,56	$_B$TiO$_2$: Ag-3	16,226	–	142,2 ± 31,7	142,8 ± 67,58	0,283	67,7 ± 11,1

−24.8 mV for $_A$TiO$_2$:Cu-3 Nps (Fig. 5 E), but PdI (Polydispersity Index) and d_{DLS} are notably increased (Table 1). This aggregation can be attributed to the possible formation of CuO species, mentioned in structural analysis.

Plain Ag Nps present substantially higher d_{DLS} (~39.9 nm) than d_{TEM} ~8.6 nm (Table 1, Fig. S3), while maintaining an extremely negative ζ value at −49.8 mV, a profile that can be explained by the existence of the large and negatively charged TA molecules attached on the surface. As for $_B$TiO$_2$:Ag Nps the ζ potential considerably decreases while PdI and d_{DLS} improve (Fig. 5F–Table 1), by increasing Ag deposition, with $_B$TiO$_2$:Ag-3 attaining a value of −67.7 mV. Consequently, by increasing the amount of Ag Nps incorporation on $_B$TiO$_2$ the colloidal behavior is improved.

3.3. Optical properties

UV-DRS spectra, in absorbance and reflectance mode, were acquired to elucidate the optical properties of the nanocomposites and their responsiveness to visible light irradiation. The deep UV absorption band present in all samples is assigned to TiO$_2$ and specifically to the electronic transition from the valence band (VB) comprising of the O $2p$ states to the conduction band (CB) of TiO$_2$ consisting of the Ti $3d$ state [102].

Cu-modified $_A$TiO$_2$ samples exhibit three additional absorption bands located at 380–420 nm (shoulder), 420–570 nm (tail), and 600–950 nm (broader band) (Fig. 5A and B). Taking into consideration the XPS results for the sample $_A$TiO$_2$:Cu-1, additional absorption bands assigned either to the LSPR effect of metallic Cu nanoparticles or the band gap transition of Cu$_2$O can be included in the 600–900 nm region of the absorbance spectra [103,104]. However due to the minimal presence of these species on the surface of $_A$TiO$_2$ their contribution does not not significantly affect the overall absorption spectra. The calculation of disorder induced energy levels below the CB of TiO$_2$, also known as Urbach energy, revealed an upward trend for the $_A$TiO$_2$:Cu Nps (107 meV < 679 meV < 942 meV < 1436 meV) following the increase in copper concentration, thus confirming that interstitial or substitutional doping of the $_A$TiO$_2$ lattice is at play. Increasing concentration of Cu resulted in an amplified intensity of the other absorption bands, suggesting their association with the interaction between Cu ions and TiO$_2$ lattice or the formation of a new phase. These defects, which are usually oxygen vacancies located close to the newly inserted Cu^{2+} ions, can create energy states between the VB and CB of TiO$_2$, redshifting the absorbance, thus rendering the semiconductor responsive to visible light [83,105,106]. The calculation of each state's energy, also known as Urbach energy, for the $_A$TiO$_2$:Cu Nps revealed an upward trend (107 meV < 679 meV < 942 meV < 1436 meV) following the increase in copper concentration, thus confirming that interstitial or substitutional doping of the $_A$TiO$_2$ lattice is at play (Fig. S6) [83, 107]. The tail at 420–570 nm corresponds to a similar trend and may be attributed to the formation of amorphous copper (II) oxide (CuO), copper (II) hydroxide (Cu(OH)$_2$ or Cu^{2+} clusters covalently bound on the acidic Ti^{4+} sites on the surface of $_A$TiO$_2$ nanoparticles [108–110]. Additionally the broad absorption at longer wavelengths is the characteristic d – d ($^2E_g \rightarrow {}^2T_{2g}$) transition of Cu^{2+} (d^9) present in the octahedral coordination environment of crystalline anatase [83]. Similar to $_A$TiO$_2$, the absorption edge of $_B$TiO$_2$ is located at 393 nm (Fig. 5D and E), suggesting that the optical properties of the prevailing anatase phase remain unaffected despite the presence of 1 % brookite phase, found in pXRD. In the case of $_B$TiO$_2$:Ag-1, 2, 3 Nps the absorption and reflection curves reveal another mechanism of modification. The absence of absorbance, which could be attributed to lattice-disruption defects, excludes Ag $^+$ doping as a modification mechanism but rather further validates that Ag is present in the form of nanoparticles on the surface of $_B$TiO$_2$. This assumption is in good agreement with the results obtained from pXRD, Raman, and TEM. The other prominent absorption in the UV-DRS spectra, which is associated with the increase in Ag concentration, is located at 400–700 nm and can be attributed to Ag Nps' LSPR triggered by the incident light. The plasmonic effect of Ag Nps can enhance the absorption of TiO$_2$ in visible light by acting as a hot electron channel through the Schottky barrier formed at the heterojunction between plasmonic Ag Nps and $_B$TiO$_2$ Nps [111,112].

The characteristic LSPR absorption peak of plain Ag Nps (Fig. S3 C) appears at 433 nm, whilst a red-shift is observed when Ag Nps are concurrently formed and embedded with $_B$TiO$_2$. As Ag concentration is increased, λ_{max} of the LSPR-assigned absorption shifts from 576 nm for $_B$TiO$_2$:Ag-1, to 604 nm for $_B$TiO$_2$:Ag-2, and 630 nm for $_B$TiO$_2$:Ag-3. LSPR absorption's λ_{max} and FWHM of plasmonic Ag Nps depend on their size, shape, and distribution; size increase causes redshift while aggregation results in peak broadening [113]. Accordingly, this redshift indicates either aggregation of the deposited Ag Nps or a wider scattered coverage of $_B$TiO$_2$ with Ag Nps,

resulting in a larger perceived size, as Ag deposition is increased. Since the colloidal behavior was proven to ameliorate from $_B$TiO$_2$: Ag-1 to $_B$TiO$_2$:Ag-3, it can be assumed that the latter argument must be at play. Additionally, an important redshift in the absorption maxima of TiO$_2$ to 330 nm is also noted for the sample $_B$TiO$_2$:Ag-3 and can be attributed to lattice defects of anatase TiO$_2$ and interparticle interactions of TiO$_2$ and Ag Nps [114]. Kubelka-Munk plots for $_A$TiO$_2$:Cu Nps and $_B$TiO$_2$:Ag Nps were constructed by transforming the reflectance curves, for the calculation of the indirect band gaps (Fig. 6C–F and Fig. S7) [115]. By employing this method we aim to unravel the extent of TiO$_2$'s bandgap modification stemming from Cu or Ag.

In the case of $_A$TiO$_2$ and its Cu-modified analogs, the bandgap energy exhibits a downward trend from 3.25 eV of the bare $_A$TiO$_2$ to 3.05 eV for $_A$TiO$_2$:Cu-3. In parallel, the increase in intensity and width of the absorption tail associated with the rise in defect-induced Urbach energy (E$_u$) implies that doping is present in every Cu concentration applied. Hence, it is safe to assume that all Cu-modified photocatalysts can be activated by visible light irradiation attributed to a combination of interstitial or substitutional doping and surface modification with Cu^{2+}.

Considering bare and Ag-modified $_B$TiO$_2$ Nps, there are no significant changes in the bandgap values of the $_B$TiO$_2$:Ag-1 (3.24 eV) and $_B$TiO$_2$:Ag-2 (3.26 eV) samples, as compared to bare $_B$TiO$_2$ (3.24 eV) and the interband transition absorption of anatase, suggesting that there is no doping present, as an additional verification to previous observations. Instead, the decoration of plasmonic Ag Nps on the surface of TiO$_2$ can directly transport electrons to the CB of TiO$_2$ rendering it active under visible light irradiation. $_B$TiO$_2$:Ag-3 Nps exhibit a noticeable decline in bandgap energy (3.08 eV) paired with the most intense absorption in the visible light originating from the LSPR effect of Ag nanoparticles. Though the doping of some portion of Ag$^+$ ions inside the lattice of TiO$_2$ cannot be entirely ruled out, most likely the redshift in absorbance maxima derives from the combined effect of the presence of smaller-sized Ag Nps, amorphous Ti(OH)$_4$ and anatase TiO$_2$. The junction of all three components may trap electrons generated from the plasmon resonance of Ag Nps and subsequently enhance the charge separation at the interface of anatase TiO$_2$ and amorphous Ti(OH)$_4$.

3.3.1. Photodegradation of MB

Fig. 3 Optical characterization of $_A$TiO$_2$(:Cu-1, 2, 3) and $_B$TiO$_2$(:Ag-1, 2, 3). (A, D); Kubelka-Munk absorption curves of $_A$TiO$_2$(:Cu-1, 2, 3) and $_B$TiO$_2$(:Ag-1, 2, 3). The inset in the top right indicates the shifting of the absorption edge with increasing the modifier's concentration. (B, E) Reflectance curves $_A$TiO$_2$(:Cu-1, 2, 3) and $_B$TiO$_2$(:Ag-1, 2, 3) (C, F) Transformed Kubelka-Munk for the calculation of the bandgap energy. E_{Bg} stands for *bandgap energy* and E$_u$ for Urbach energy.

To examine the photocatalytic prowess of the synthesized nanostructures, in solution, we studied the degradation of MB dye under visible light (LED 20W) irradiation. Their adsorption capacity was also evaluated to assess the interactions of the samples with the dye prior to illumination.

Cu-doped $_A$TiO$_2$ Nps can be activated under visible light to generate ROS i.e. $\cdot$O$_2^-$ and $\cdot$OH which next oxidize MB to H$_2$O and CO$_2$ [116]. The degradation rate constants K$_{deg}$ (Table 2), calculated from the kinetic study plots (Fig. 7A and B), reveal that $_A$TiO$_2$:Cu-1 is the most active, as it accomplished almost complete decomposition of MB. As soon as irradiation begins the reaction follows
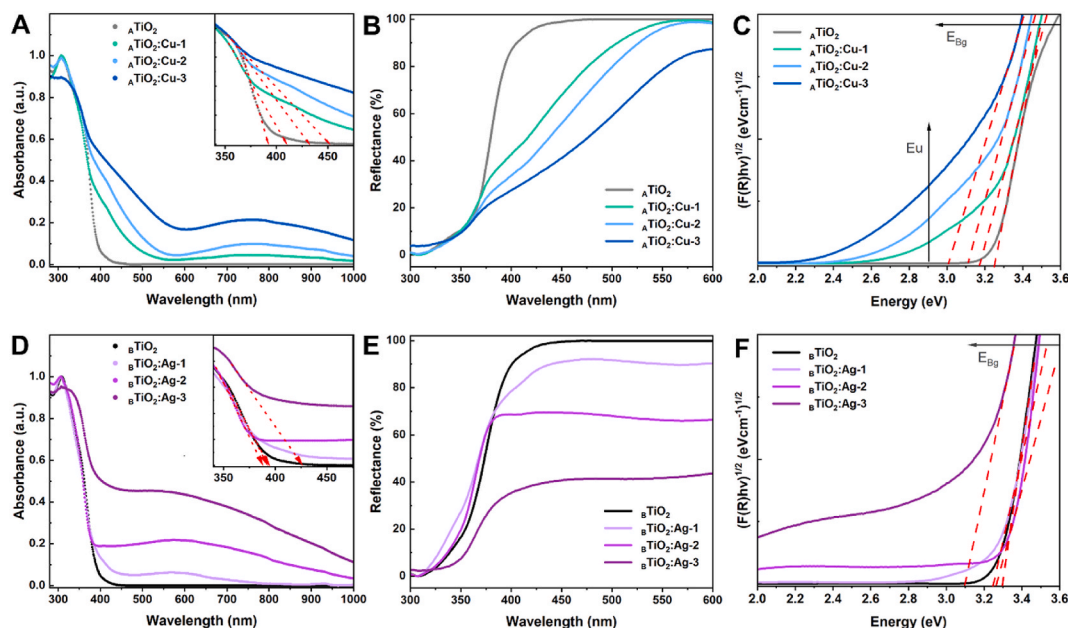
Fig. 6. Absorption curves of (A) $_A$TiO$_2$(:Cu-1, 2, 3) and (D) $_B$TiO$_2$(:Ag-1, 2, 3); inset in the top right indicates the absorption edge shift with increasing concentration of Cu or Ag modifiers. Reflectance curves of (B) $_A$TiO$_2$(:Cu-1, 2, 3) and (E) $_B$TiO$_2$(:Ag-1, 2, 3). Kubelka-Munk-transformed reflectance curves for the calculation of the bandgap energy of (C) $_A$TiO$_2$(:Cu-1, 2, 3) and (F) $_B$TiO$_2$(:Ag-1, 2, 3). E_{Bg} stands for bandgap energy and E$_u$ for Urbach energy.

Table 2

Kinetic evaluation parameters of the photocatalytic activity of $_A$TiO$_2$(:Cu-1, 2, 3) and $_B$TiO$_2$(:Ag-1, 2, 3) derived from the MB degradation study.

Sample	D(%)	K_{deg} (10^{-3}) (s^{-1})	$t_{1/2}$	Sample	D(%)	K_{deg} (10^{-3}) (s^{-1})	$t_{1/2}$
$_A$TiO$_2$	71.7	3.5	198	$_B$TiO$_2$	92.9	7.9	88
$_A$TiO$_2$:Cu-1	94.4	9	77	$_B$TiO$_2$:Ag-1	88.4	6.7	103
$_A$TiO$_2$:Cu-2	81.9	7	99	$_B$TiO$_2$:Ag-2	97.7	12.2	57
$_A$TiO$_2$:Cu-3	87.7	6.2	112	$_B$TiO$_2$:Ag-3	92.9	8.7	80
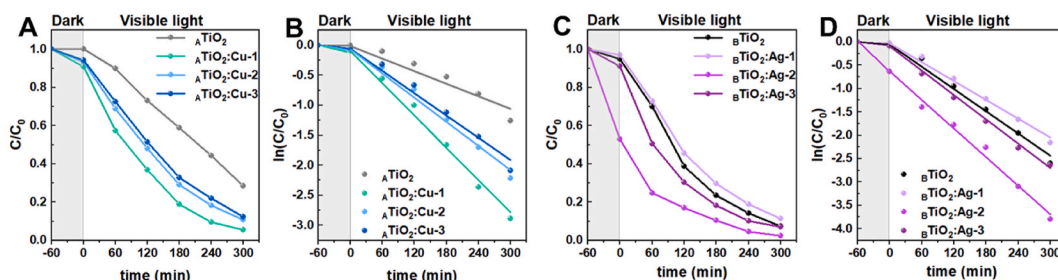
Fig. 7. Photocatalytic degradation of MB under visible light irradiation: {C/C$_0$ (time)} and linearly fitted {ln(C/C$_0$) (time)} plots of (A,B) $_A$TiO$_2$(:Cu-1, 2, 3) Nps and (C,D) $_B$TiO$_2$(:Ag-1, 2, 3) Nps.

pseudo-first-order kinetics. There was no significant adsorption capacity of MB on either of the $_A$TiO$_2$(:Cu-1,2,3) Nps, implying that the degradation involves only the photocatalytic pathway, ruling out any other possible side reactions that would induce error in the experimental results. The increased photocatalytic ability of $_A$TiO$_2$:Cu-1 implies that the copper species present on the surface of TiO$_2$ at this copper loading (Cu^0 or Cu$^+$) can facilitate more efficient charge separation and electron transfer to MB dye, while the increase of Cu^{2+} related species on the surface of TiO$_2$, at higher Cu loadings, have an adverse effect on the photocatalytic activity of the hybrid photocatalyst. This result comes in agreement with previous studies [85,117,118]. While the UV-DRS study implies that $_A$TiO$_2$:Cu-3 has better responsiveness to visible light, instead it seems that the large generation of surface-embedded clusters of Cu^{2+} or amorphous Cu(OH)$_2$ could act as recombination sites for the photogenerated electrons and positively charged holes (h$^+$) [119,120]. In the case of $_B$TiO$_2$(:Ag-1, 2, 3) (Fig. 7C and D) the bare $_B$TiO$_2$ shows a rise in visible-light-induced photocatalytic activity when compared to $_A$TiO$_2$.

The cluster-like shape of $_B$TiO$_2$ could be described as having cavities or pores which would result in an increased effective surface-to-volume ratio, thus offering accessible sites for molecular diffusion or adsorption as well as enhanced light harvesting properties owing to multiple internal reflections of the incident light [121]. $_B$TiO$_2$:Ag-2 (Table 1) showed intrinsic adsorption capacity for MB in
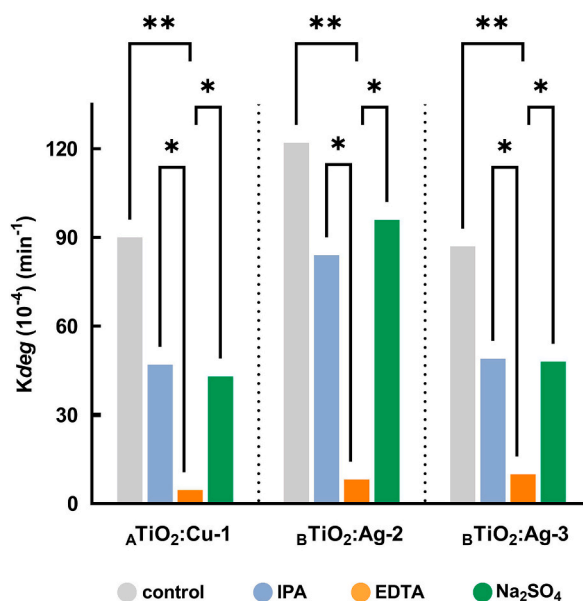
Fig. 8. Effect of radical scavengers IPA, EDTA and Na$_2$SO$_4$ on the degradation rate constant (Kdeg) of the selected photocatalysts. Statistical analysis of the results is based on a 2-way ANOVA multiple comparisons test within the different sets of samples, with ****(p $\leq$ 0.0001), *** (p $\leq$ 0.001), **(p $\leq$ 0.01), * (p $\leq$ 0.05).

the dark, compared to $_BTiO_2$:Ag-1 and 3. The increased photodegradation rate, of both $_BTiO_2$:Ag-2 and $_BTiO_2$:Ag-3, can be attributed to the adsorption of the dye on the surface of the modified TiO_2 Nps and to synergistic effects between the transfer of hot electrons from the LSPR of Ag Nps, respectively. The increased degradation rate of MB using the modified nanoparticles under illumination from low-wattage visible-light LED lamps indicates their potential for use as indoor antipollution agents.

3.3.2. Determination of reactive species in photocatalysis

Visible-light absorption from the Cu-doped and Ag-decorated photocatalysts leads to electronic excitation (e^-) to the conduction band (CB) of TiO_2 or the mid-gap states induced by the dopant while leaving a positive charged hole (h^+) in the valence band (VB). These charge carriers are the driving force of photocatalysis and further reactions with H_2O or O_2 dissolved in water generates the Reactive Oxygen Species (ROS) that lead to the degradation of pollutants. The reactions taking place can be described with the following pathways:

$$_{\cdot A,B}TiO_2 : Cu, Ag \xrightarrow{\textit{Visible Light}} e^-(CB) + h^+(VB) \tag{8}$$

$$H_2O + h^+(VB) \rightarrow \ .^\bullet OH + H^+ \tag{9}$$

$$O_2 + e^-(CB) \rightarrow O_2^{\bullet-} \tag{10}$$

$$O_2^{\bullet-} + H^+ \rightarrow \ .^\bullet OOH \tag{11}$$
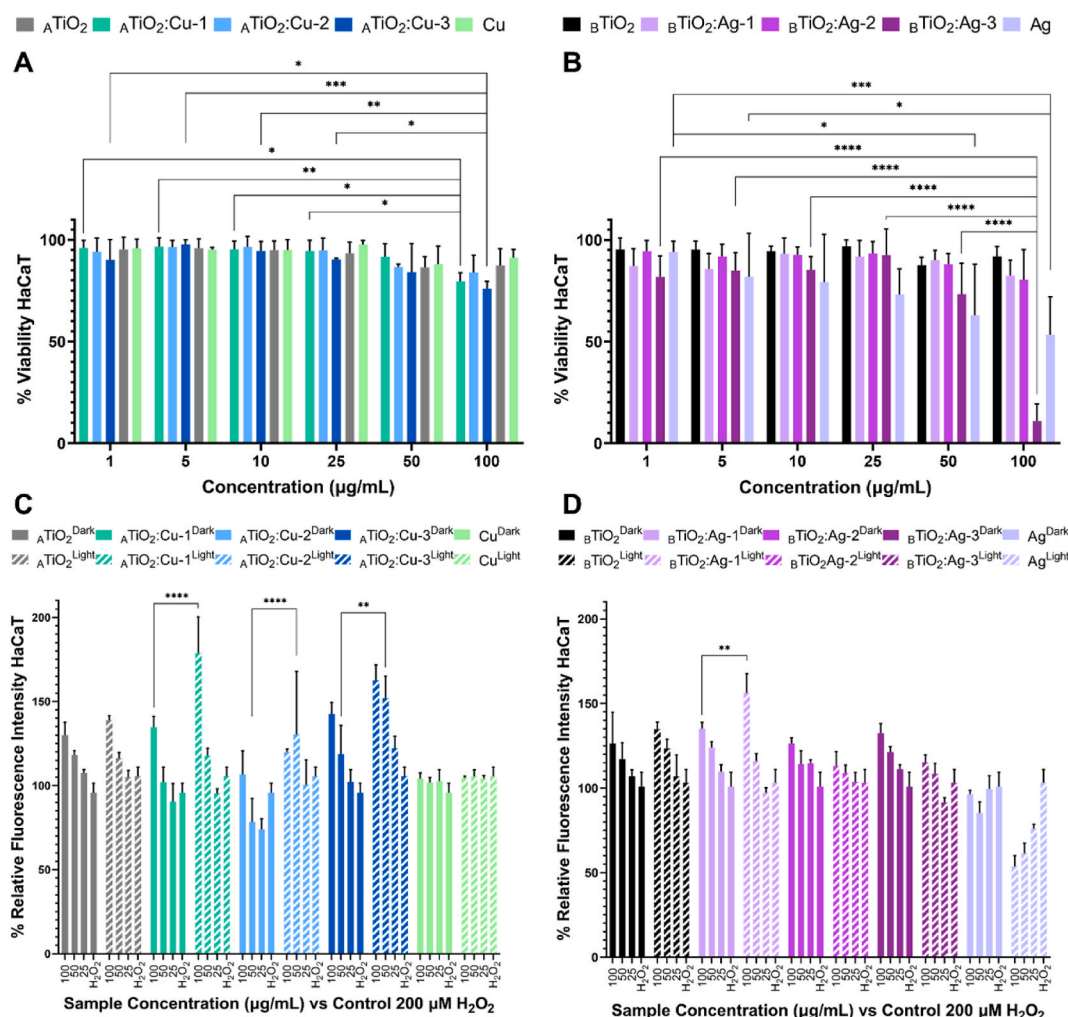
Fig. 9. MTT assay on HaCaT cell line after treatment with (A) $Cu(NO_3)_2.3H_2O$ and $_ATiO_2$ (:Cu-1,2,3) Nps and (B) Ag and $_BTiO_2$(:Ag-1,2,3) Nps. ROS assay results expressed as %Relative Fluorescent Intensity after incubation, in dark or under visible light irradiation, with (C) $Cu(NO_3)_2$ and $_ATiO_2$ (:Cu-1,2,3) Nps and (D) Ag and $_BTiO_2$(:Ag-1,2,3) Nps.

$$Pollutant + h^+ (VB) \rightarrow Oxidized\ pollutant \tag{12}$$

$$Pollutant + e^- (CB) \rightarrow Reduced\ pollutant \tag{13}$$

In the case of Cu-doped TiO_2 catalysts, $_ATiO_2$:Cu-1 was selected due to its better photocatalytic performance in MB degradation. For Ag-modified TiO_2, $_BTiO_2$:Ag-2 and $_BTiO_2$:Ag-3 photocatalysts were selected to investigate whether Ag decoration and doping of the TiO_2 lattice, respectively, affect the dominant radical species responsible for dye degradation. The results of the reactive species scavenging experiment for each photocatalyst are presented in Fig. 8, where the degradation constants ($Kdeg$) of MB in the presence and absence (control) of each radical scavenger are compared.

As evidenced, EDTA had the largest negative impact on the degradation kinetics of all photocatalysts as the degradation constant diminished to the values of $4.6 \cdot 10^{-4}$, $8.2 \cdot 10^{-4}$, and $9.9 \cdot 10^{-4}$ for the Cu doped sample and $_BTiO_2$:Ag-2 and $_BTiO_2$:Ag-3 respectively. This result implies that the main active species contributing to the oxidation of MB are the positively charged holes (h^+) generated at the VB of the photocatalysts. Hydroxyl radicals ($^\bullet OH$) scavenging and free electron (e^-) resulted in a less important decline in the degradation rate for the selected photocatalysts. This should be replaced by the following: Considering the difference between the means of $Kdeg$ values (based on the multi-comparison confidence interval plot of the two-way ANOVA statistical analysis-Fig. S8), $_BTiO_2$:Ag-2 showed substantial $kdeg$ increase compared to $_BTiO_2$:Ag-3. This result further supports the different modification mechanisms present in these two samples.

3.4. Biocompatibility and safety assessment under visible light irradiation

The biocompatibility of all prepared samples was assessed through the MTT assay on HaCaT cells at varying concentrations (Fig. 9A and B). Plain $_ATiO_2$ and $_BTiO_2$ did not inhibit cellular proliferation at the tested concentrations. According to the statistical analysis within each sample, highly and extremely significant toxicity is exhibited at the highest concentration of $_ATiO_2$:Cu-3 Nps or $_BTiO_2$:Ag-3 Nps, respectively. Among the different samples, no significant effect is observed, except in the case of 100 μg/ml $_BTiO_2$:Ag-3 Nps, where there is an extremely significant difference compared to the other samples at the same concentration. Plain Ag Nps exhibit concentration-dependent toxicity. The observed trend of decreasing cellular proliferation seems to be related to the increasing percentage of metal, Cu or Ag, incorporated in the structure. Both hybrid materials exhibit comparable behavior, except for $_BTiO_2$:Ag-3 Nps at the highest concentration, which is significantly more toxic than the other samples at 100 μg/ml.

The potential activity of hybrid titania materials to induce the production of ROS on HaCaT cells was investigated through the established method of H_2DCFDA. Both fluorescent spectroscopy (Fig. 9C and D) and microscopy (Fig. S11) attested to the inherent ability of the tested samples to produce ROS, after incubation with the cells for 4 h at 37 °C without (dark) or under visible light irradiation (light). According to a multivariant statistical analysis of the data collected from the *in vitro* spectroscopic assay, pure $_ATiO_2$, and $_BTiO_2$ Nps' ROS production remained the same between dark and light conditions, whereas hybrid nanoparticles presented a different profile (Fig. 9C and D). As a first remark, there is a noticeable trend of decreasing ROS production with the decrease of sample concentration during incubation, but most samples demonstrated higher values than the control sample treated with H_2O_2. In more detail, under visible light irradiation, an extremely significant increase in ROS production was detected for all three samples of $_ATiO_2$:Cu, but only $_BTiO_2$:Ag-1 Nps demonstrated a highly significant result, whereas the rest of $_BTiO_2$:Ag Nps had similar or less compared to the dark. To delve more into this peculiar behavior, a complementary MTT assay was performed, in the same cell culture plates right after ROS assay (Fig. S12). In the case of $_BTiO_2$:Ag Nps there is a noticeable decrease in viability after light irradiation compared to samples that remained in the dark, which could explain the peculiar ROS production trend. This effect was not as significant in the case
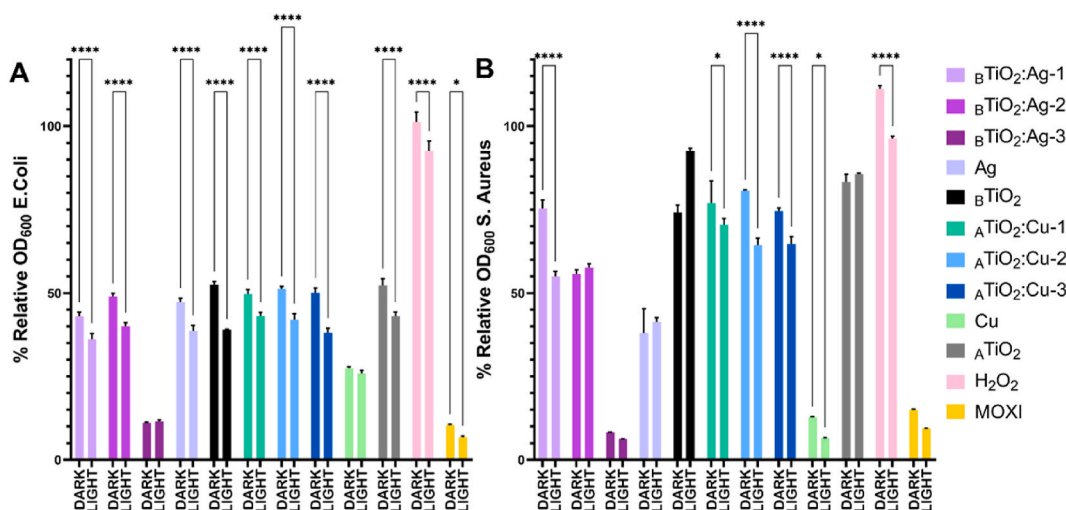
Fig. 10. %Relative OD_{600} after overnight exposure in the dark or under light irradiation of A) *E. coli* and B) *S. aureus* with the nanostructures.

of $_A$TiO$_2$:Cu samples, thus ROS production was evidenced unhindered.

Fluorescent microscopy gave a visual insight into ROS production stimulated by the samples on live cell cultures after treatment with H$_2$DCFDA, under the same experimental conditions. To avoid potential toxicity, cells were treated with the nanostructures at the intermediate concentration of 50 μg/ml. Double negative (untreated-unstained), negative (untreated-stained), and positive (H$_2$O$_2$ treated-stained) were used as reference to evaluate the treated samples. Indeed, cells treated with $_A$TiO$_2$:Cu Nps under light irradiation demonstrated a more intense and localized fluorescent signal, compared to the samples that remained in the dark (Fig. S12).

Interestingly, all cells treated with $_B$TiO$_2$:Ag Nps demonstrated a highly intense signal as well (Fig. S11), despite the spectroscopic results, further validating the hypothesis that, due to decreased viability, the overall fluorescent signal was arrested. The negative control demonstrated scattered fluorescent signal, mostly in the exterior of the cells, which has been previously mentioned in literature, as artefactual signals could be a drawback of this method, and was taken into consideration in our analysis [122,123].

In more detail, the fluorescence of cells treated with $_A$TiO$_2$:Cu-1 was more intense after light irradiation than the other two samples with higher Cu concentration. Interestingly, taking into account the structural and photocatalytic response data, it seems like more Cu ions are readily available to be released in the cell for $_A$TiO$_2$:Cu-2, compared to $_A$TiO$_2$:Cu-1. When Cu(NO$_3$)$_2$•3H$_2$O (hereinafter referred to as Cu) was used as a reference, to elucidate pure Cu^{2+} ions' effect on the cells, the intense diffused signal, after dark incubation, appeared more localized after light irradiation, validating the generation of ROS even in the dark. Cells treated with $_A$TiO$_2$:Cu-3 demonstrated minute fluorescence, evidenced in both spectroscopic and microscopic results, which could correlate with the least photocatalytic activity among the sample group of $_A$TiO$_2$:Cu Nps.

To further examine the propensity of $_B$TiO$_2$:Ag Nps sample group to produce ROS, the effect of plain Ag Nps should be taken into consideration. From the fluorescent microscopy images, cells treated with Ag Nps in the dark exhibited localized fluorescent spots, whereas after light irradiation the signal was significantly amplified, revealing the propagation of ROS stimulated by Ag Nps. Therefore, the amplified fluorescent signal, as the Ag incorporation on $_B$TiO$_2$ Nps increases, can be ascribed to the generation of ROS due to photocatalytic enhancement supported by the optical response data of these samples.

Taking all the results of biocompatibility assessment into consideration, distinct conclusions can be drawn. At a concentration of 50 μg/ml or less, both $_A$TiO$_2$:Cu and $_B$TiO$_2$:Ag can be declared safe for contact with human skin cells. A possible route of toxicity for higher concentrations is through oxidative stress, especially in the case of higher %wt of Cu or Ag on titania after light irradiation at the highest concentration. Considering that these hybrid nanomaterials are intended to be used as additives in construction materials, such as paints for indoor surface sanitation, when in contact with the skin the bioavailability is significantly low.

3.5. Antimicrobial activity

The effect of 24 h visible light irradiation on the antimicrobial activity of the Cu and Ag-modified titania nanostructures was evaluated in liquid cultures of *E. coli* (Gram-negative) and *S. aureus* (Gram-positive). *E. coli* demonstrated an overall decreased % Relative OD$_{600}$, compared to *S. aureus*, indicating heightened sensitivity of *E. coli* to titania-modified nanostructures, in both light and dark conditions (Fig. 10).

All three $_A$TiO$_2$:Cu Nps exhibited an extremely significant effect after light irradiation in the case of *E. coli*, similarly with $_B$TiO$_2$:Ag-1, $_B$TiO$_2$:Ag-2, and Ag Nps. An extremely significant decrease of %Relative OD$_{600}$, after light irradiation was observed in the case of *S. aureus* as well, for the samples treated with $_A$TiO$_2$:Cu-2, $_A$TiO$_2$:Cu-3, and $_B$TiO$_2$:Ag-1. $_B$TiO$_2$:Ag-3 demonstrated an extremely significant bactericidal activity in both bacterial strains, even in the dark, rendering the evaluation of light impact insignificant, at the tested concentration.

The antibacterial effect of the nanostructures could be attributed to different bactericidal or bacteriostatic mechanisms induced by the tested nanostructures [59,124]. Herein, the probability of ROS production was assessed via fluorescent microscopy (Fig. S11 and Fig. S12) and spectroscopy (Fig. S.10) after treatment with H$_2$DCFDA. Fluorescence microscopy images verified the production of ROS after light irradiation in the case of *E. coli* treated with the modified titania nanostructures whereas weak signal was observed from plain $_A$TiO$_2$ and $_B$TiO$_2$. It can be assumed that the increased antimicrobial effect observed after measuring the %Relative OD$_{600}$ can be attributed to ROS generation stemming from light activation. *S. aureus* samples, treated with the same nanostructures, demonstrated moderate fluorescence which can be correlated to the higher %Relative OD$_{600}$, compared to *E. coli*. Hence, there is a direct association between antimicrobial activity and enhanced ROS production. Summarizing the antimicrobial activity results, we propose a direct photocatalytically driven biocidal impact by increasing %wt of Cu or Ag on $_A$TiO$_2$ or $_B$TiO$_2$, respectively. The generation of ROS as a potential antibacterial mechanism enhanced by visible light irradiation can be verified, while a selectivity towards *E. coli* is indicated.

4. Conclusions

Two distinct experimental procedures were developed for the synthesis of both bare and modified TiO$_2$ nanoparticles. An easily upscalable solvothermal method was employed for the synthesis of Cu^{2+} doped TiO$_2$ Nps, whilst a simple one-pot green sol-gel approach was applied for the fabrication of bare and Ag-decorated TiO$_2$ Nps. The first method procured smaller, highly crystalline, nanoparticles around 20 nm, compared to the second method which rendered cluster-like nanostructures of around 90 nm. Comprehensive characterization was conducted to elucidate their structural, morphological, and optical properties. All samples exhibited superior responsiveness to visible light compared to bare TiO$_2$. Photocatalysts with 2.77 wt% Cu and 5.04 wt% Ag loading demonstrated the most effective anti-pollution efficacy for MB dye, under visible light illumination ($\lambda > 420$ nm). Most titania-modified nanostructures demonstrated a concentration-dependent effect on HaCaT cellular viability whilst proving to be biocompatible for up to 50 μg/ml per MTT assay results. Cellular and microbial ROS generation was enhanced following visible light irradiation and was correlated with

structural and morphological differences among the samples. Photocatalytic-driven antimicrobial activity of the synthesized nano-structures was verified by the significantly decreased %RelativeOD600 values of E. coli and S. aureus incubated under visible light illumination ($\lambda > 400$ nm), compared to those in the dark. In conclusion, our results suggest that Cu-doped $_A$TiO$_2$ and Ag-decorated $_B$TiO$_2$ could serve as efficient antipollution and antibacterial agents, by monitoring the fraction of the metal-modified titania.

As the need for sanitation of indoor spaces (hospitals, restaurants, and transportation) is becoming more and more demanding due to overpopulation, the potential applications of these hybrid materials are vast, in the field of construction materials, paints, and surface coatings, while taking advantage of their photocatalytic activity under the abundantly available visible light radiation from visible light LED lamps. Future perspectives include real-life applications to assess the precise impact of the visible light-activated hybrid titania nanoparticles synthesized herein as sustainable biocidal additives that can replace commonly used toxic substances.

Data availability

Data available upon reasonable request.

CRediT authorship contribution statement

Panagiotis Tzevelekidis: Writing – original draft, Investigation, Formal Analysis, Data Curation, Visualization. **Maria Theodo-siou:** Writing – original draft, Investigation, Formal Analysis, Data Curation, Visualization. **Athina Papadopoulou:** Investigation. **Elias Sakellis:** Investigation. **Nikos Boukos:** Resources. **Alexandros K. Bikogiannakis:** Investigation. **Georgios Kyriakou:** Investigation, Resources. **Eleni K. Efthimiadou:** Project Administration, Funding Acquisition, Conceptualization, Supervision, Resources, Methodology, Writing – Review & Editing. **Christiana A. Mitsopoulou:** Project Administration, Funding Acquisition, Conceptualization, Supervision, Resources, Methodology, Writing – Review & Editing.

Declaration of competing interest

We have no conflict of interest to declare.

Acknowledgments

Appendix A. Supplementary data

Supplementary data to this article can be found online at https://doi.org/10.1016/j.heliyon.2024.e35634.

References

[1] H. Chawla, P. Anand, K. Garg, N. Bhagat, S.G. Varmani, T. Bansal, A.J. McBain, R.G. Marwah, A comprehensive review of microbial contamination in the indoor environment: sources, sampling, health risks, and mitigation strategies, Front. Public Health 11 (2023) 1285393, https://doi.org/10.3389/FPUBH.2023.1285393/BIBTEX.

[2] A. Nieto-Márquez, M. de Mateo, A. Barrios, M.d.M. de la Fuente García-Soto, A. Narros, Improving indoor air quality by using photocatalytic paints. Real scale study at the Technical University of Madrid, Atmos. Pollut. Res. 14 (2023) 101827, https://doi.org/10.1016/J.APR.2023.101827.

[3] S. Velazquez, W. Griffiths, L. Dietz, P. Horve, S. Nunez, J. Hu, J. Shen, M. Fretz, C. Bi, Y. Xu, K.G. Van Den Wymelenberg, E.M. Hartmann, S.L. Ishaq, From one species to another: a review on the interaction between chemistry and microbiology in relation to cleaning in the built environment, Indoor Air 29 (2019) 880, https://doi.org/10.1111/INA.12596.

[4] W. Bäumler, D. Eckl, T. Holzmann, W. Schneider-Brachert, Antimicrobial coatings for environmental surfaces in hospitals: a potential new pillar for prevention strategies in hygiene, Crit. Rev. Microbiol. 48 (2022) 531–564, https://doi.org/10.1080/1040841X.2021.1991271.

[5] P. Ganguli, S. Chaudhuri, Nanomaterials in antimicrobial paints and coatings to prevent biodegradation of man-made surfaces: a review, Mater Today Proc 45 (2021) 3769–3777, https://doi.org/10.1016/J.MATPR.2021.01.275.

[6] M. Schutte-Smith, E. Erasmus, R. Mogale, N. Marogoa, A. Jayiya, H.G. Visser, Using visible light to activate antiviral and antimicrobial properties of TiO$_2$ nanoparticles in paints and coatings: focus on new developments for frequent-touch surfaces in hospitals, J Coat Technol Res 20 (2023) 789, https://doi.org/10.1007/S11998-022-00733-8.

[7] M. Janczarek, Ł. Klapiszewski, P. Jędrzejczak, I. Klapiszewska, A. Ślosarczyk, T. Jesionowski, Progress of functionalized TiO$_2$-based nanomaterials in the construction industry: a comprehensive review, Chem. Eng. J. 430 (2022) 132062, https://doi.org/10.1016/J.CEJ.2021.132062.

[8] A. Fujishima, K. Honda, Studies on photosensitive electrode reactions .3. Electrochemical evidence for mechanism of primary stage of photosynthesis, Bull. Chem. Soc. Jpn. 44 (1971) 1148–1150.

[9] A. Seretis, P. Diamantopoulou, I. Thanou, P. Tzevelekidis, C. Fakas, P. Lilas, G. Papadogianakis, Recent advances in ruthenium-catalyzed hydrogenation reactions of renewable biomass-derived levulinic acid in aqueous media, Front. Chem. 8 (2020) 1–22, https://doi.org/10.3389/fchem.2020.00221.

[10] A. Fujishima, K. Honda, Studies on photosensitive electrode reactions .3. Electrochemical evidence for mechanism of primary stage of photosynthesis, Bull. Chem. Soc. Jpn. 44 (1971) 1148–1150.

[11] K. Maeda, K. Domen, Photocatalytic water splitting: recent progress and future challenges, J. Phys. Chem. Lett. 1 (2010) 2655–2661, https://doi.org/10.1021/jz1007966.

[12] G. Li, N.M. Dimitrijevic, L. Chen, T. Rajh, K.A. Gray, Role of surface/interfacial Cu2+ sites in the photocatalytic activity of coupled CuO-TiO2 nanocomposites, J. Phys. Chem. C 112 (2008) 19040–19044, https://doi.org/10.1021/jp8068392.

[13] A.M. Beyene, M. Moniruzzaman, A. Karthikeyan, T. Min, Curcumin nanoformulations with metal oxide nanomaterials for biomedical applications, Nanomaterials 11 (2021) 1–25, https://doi.org/10.3390/nano11020460.

[14] J.S. Boateng, K.H. Matthews, H.N.E. Stevens, G.M. Eccleston, Wound healing dressings and drug delivery systems: a review, J Pharm Sci 97 (2008) 2892–2923, https://doi.org/10.1002/jps.21210.

[15] F.U. Rehman, C. Zhao, H. Jiang, X. Wang, Biomedical applications of nano-titania in theranostics and photodynamic therapy, Biomater. Sci. 4 (2016) 40–54, https://doi.org/10.1039/c5bm00332f.

[16] Y. Yan, C. Soraru, V. Keller, N. Keller, L. Ploux, Antibacterial and biofilm-preventive photocatalytic activity and mechanisms on P/F-modified TiO2 coatings, ACS Appl. Bio Mater. 3 (2020) 5687–5698, https://doi.org/10.1021/acsabm.0c00467.

[17] A. Nikpasand, M.R. Parvizi, Evaluation of the effect of titatnium dioxide nanoparticles/gelatin composite on infected skin wound healing; an animal model study, Bull Emerg Trauma 7 (2019) 366–372, https://doi.org/10.29252/beat-070405.

[18] M.Z. Ahmad, A.S. Alasiri, J. Ahmad, A.A. Alqahtani, M.M. Abdullah, B.A. Abdel-Wahab, K. Pathak, R. Saikia, A. Das, H. Sarma, S.A. Alzahrani, Green synthesis of titanium dioxide nanoparticles using ocimum sanctum leaf extract: in vitro characterization and its healing efficacy in diabetic wounds, Molecules 27 (2022) 1–17, https://doi.org/10.3390/molecules27227712.

[19] J. Zhao, J. Xu, X. Jian, J. Xu, Z. Gao, Y.Y. Song, NIR light-driven photocatalysis on amphiphilic TiO2 nanotubes for controllable drug release, ACS Appl. Mater. Interfaces 12 (2020) 23606–23616, https://doi.org/10.1021/acsami.0c04260.

[20] T. Luttrell, S. Halpegamage, J. Tao, A. Kramer, E. Sutter, M. Batzill, Why is anatase a better photocatalyst than rutile? - model studies on epitaxial TiO2 films, Sci. Rep. 4 (2015) 1–8, https://doi.org/10.1038/srep04043.

[21] D. Wang, D. Choi, J. Li, Z. Yang, Z. Nie, R. Kou, D. Hu, C. Wang, L. V Saraf, J. Zhang, I.A. Aksay, J. Liu, Self-Assembled TiO2 – Graphene Hybrid Insertion, vol. 3, 2009, pp. 907–914.

[22] D. Chen, F. Huang, Y.B. Cheng, R.A. Caruso, Mesoporous anatase TiO2 beads with high surface areas and controllable pore sizes: a superior candidate for high-performance dye-sensitized solar cells, Adv. Mater. 21 (2009) 2206–2210, https://doi.org/10.1002/adma.200802603.

[23] X. Wu, S. Yin, Q. Dong, B. Liu, Y. Wang, T. Sekino, S.W. Lee, T. Sato, UV, visible and near-infrared lights induced NOx destruction activity of (Yb,Er)-NaYF4/C-TiO2 composite, Sci. Rep. 3 (2013) 1–8, https://doi.org/10.1038/srep02918.

[24] T. Luttrell, S. Halpegamage, J. Tao, A. Kramer, E. Sutter, M. Batzill, Why is anatase a better photocatalyst than rutile? - model studies on epitaxial TiO2 films, Sci. Rep. 4 (2015) 1–8, https://doi.org/10.1038/srep04043.

[25] S.A. Ansari, M.M. Khan, M.O. Ansari, M.H. Cho, Nitrogen-doped titanium dioxide (N-doped TiO2) for visible light photocatalysis, New J. Chem. 40 (2016) 3000–3009, https://doi.org/10.1039/c5nj03478g.

[26] K.N. Pandiyaraj, D. Vasu, R. Ghobeira, P.S.E. Tabaei, N. De Geyter, R. Morent, M. Pichumani, P.V.A. Padmanabhanan, R.R. Deshmukh, Dye wastewater degradation by the synergetic effect of an atmospheric pressure plasma treatment and the photocatalytic activity of plasma-functionalized Cu–TiO2 nanoparticles, J. Hazard Mater. 405 (2021) 124264, https://doi.org/10.1016/j.jhazmat.2020.124264.

[27] M.H.N. Assadi, D.A.H. Hanaor, The effects of copper doping on photocatalytic activity at (101) planes of anatase TiO2 : a theoretical study, Appl. Surf. Sci. 387 (2016) 682–689, https://doi.org/10.1016/j.apsusc.2016.06.178.

[28] H. Chakhtouna, H. Benzeid, N. Zari, A. el kacem Qaiss, R. Bouhfid, Recent progress on Ag/TiO2 photocatalysts: photocatalytic and bactericidal behaviors, Environ. Sci. Pollut. Control Ser. 28 (2021) 44638–44666, https://doi.org/10.1007/s11356-021-14996-y.

[29] B. Wu, R. Huang, M. Sahu, X. Feng, P. Biswas, Y.J. Tang, Bacterial responses to Cu-doped TiO2 nanoparticles, Sci. Total Environ. 408 (2010) 1755–1758, https://doi.org/10.1016/j.scitotenv.2009.11.004.

[30] B. Choudhury, M. Dey, A. Choudhury, Shallow and deep trap emission and luminescence quenching of TiO2 nanoparticles on Cu doping, Appl. Nanosci. 4 (2014) 499–506, https://doi.org/10.1007/s13204-013-0226-9.

[31] B. Choudhury, M. Dey, A. Choudhury, Defect generation, d-d transition, and band gap reduction in Cu-doped TiO2 nanoparticles, Int. Nano Lett. 3 (2013), https://doi.org/10.1186/2228-5326-3-25.

[32] R. Chauhan, A. Kumar, R.P. Chaudhary, Structural and photocatalytic studies of Mn doped TiO2 nanoparticles, Spectrochim. Acta Mol. Biomol. Spectrosc. 98 (2012) 256–264, https://doi.org/10.1016/j.saa.2012.08.009.

[33] C. Liao, Y. Li, S.C. Tjong, Visible-light active titanium dioxide nanomaterials with bactericidal properties, Nanomaterials 10 (2020), https://doi.org/10.3390/nano10010124.

[34] A. Hernández-Gordillo, V.R. González, Silver nanoparticles loaded on Cu-doped TiO2 for the effective reduction of nitro-aromatic contaminants, Chem. Eng. J. 261 (2015) 53–59, https://doi.org/10.1016/j.cej.2014.05.148.

[35] V.C. Anitha, A. Goswami, H. Sopha, D. Nandan, M.B. Gawande, K. Cepe, S. Ng, R. Zboril, J.M. Macak, Pt nanoparticles decorated TiO2 nanotubes for the reduction of olefins, Appl. Mater. Today 10 (2018) 86–92, https://doi.org/10.1016/j.apmt.2017.12.006.

[36] J. Taing, M.H. Cheng, J.C. Hemminger, Photodeposition of Ag or Pt onto TiO2 nanoparticles decorated on step edges of Hopg, ACS Nano 5 (2011) 6325–6333, https://doi.org/10.1021/nn201396v.

[37] Y. Tian, T. Tatsuma, Mechanisms and applications of plasmon-induced charge separation at TiO2 films loaded with gold nanoparticles, J. Am. Chem. Soc. 127 (2005) 7632–7637, https://doi.org/10.1021/ja042192u.

[38] M. Endo-Kimura, K. Wang, Z. Bielan, M. Janczarek, A. Markowska-Szczupak, E. Kowalska, Antibacterial activity of core-shell CuxO@TiO2 photocatalyst under UV, vis and dark, Surface. Interfac. 32 (2022), https://doi.org/10.1016/j.surfin.2022.102125.

[39] M. Amiri, K. Dashtian, M. Ghaedi, S. Mosleh, A dual surface inorganic molecularly imprinted Bi2WO6-CuO/Ag2O heterostructure with enhanced activity-selectivity towards the photocatalytic degradation of target contaminants, Photochem. Photobiol. Sci. 19 (2020) 943–955, https://doi.org/10.1039/d0pp00008f.

[40] E. Albiter, M.A. Valenzuela, S. Alfaro, G. Valverde-Aguilar, F.M. Martínez-Pallares, Photocatalytic deposition of Ag nanoparticles on TiO2: metal precursor effect on the structural and photoactivity properties, J. Saudi Chem. Soc. 19 (2015) 563–573, https://doi.org/10.1016/j.jscs.2015.05.009.

[41] Y. Li, K. Lv, W. Ho, F. Dong, X. Wu, Y. Xia, Hybridization of rutile TiO2 (rTiO2) with g-C3N4 quantum dots (CN QDs): an efficient visible-light-driven Z-scheme hybridized photocatalyst, Appl. Catal., B 202 (2017) 611–619, https://doi.org/10.1016/j.apcatb.2016.09.055.

[42] L. Wang, R. Wang, L. Feng, Y. Liu, Coupling TiO2 nanorods with g-CN using modified physical vapor deposition for efficient photoelectrochemical water oxidation, J. Am. Ceram. Soc. 103 (2020) 6272–6279, https://doi.org/10.1111/jace.17335.

[43] C.E. Housecroft, E.C. Constable, The emergence of copper(I)-based dye sensitized solar cells, Chem. Soc. Rev. 44 (2015) 8386–8398, https://doi.org/10.1039/c5cs00215j.

[44] Z.S. Wang, Y. Cui, Y. Dan-Oh, C. Kasada, A. Shinpo, K. Hara, Molecular design of coumarin dyes for stable and efficient organic dye-sensitized solar cells, J. Phys. Chem. C 112 (2008) 17011–17017, https://doi.org/10.1021/jp806927b.

[45] F. Li, K. Fan, B. Xu, E. Gabrielsson, Q. Daniel, L. Li, L. Sun, Organic dye-sensitized tandem photoelectrochemical cell for light driven total water splitting, J. Am. Chem. Soc. 137 (2015) 9153–9159, https://doi.org/10.1021/jacs.5b04856.

[46] N.R. Dhineshbabu, V. Rajendran, N. Nithyavathy, R. Vetumperumal, Study of structural and optical properties of cupric oxide nanoparticles, Appl. Nanosci. 6 (2016) 933–939, https://doi.org/10.1007/s13204-015-0499-2.

[47] D.O. Scanlon, B.J. Morgan, G.W. Watson, Modeling the polaronic nature of p -type defects in Cu2 O: the failure of GGA and GGA+U, J. Chem. Phys. 131 (2009), https://doi.org/10.1063/1.3231869.

[48] X. Qiu, M. Miyauchi, K. Sunada, M. Minoshima, M. Liu, Y. Lu, D. Li, Yoshiki Shimodaira, Y. Hosogi, Y. Kuroda, K. Hashimoto, Hybrid Cu x O/TiO 2 nanocomposites as risk-reduction materials in indoor, ACS Nano 6 (2012) 1609–1618.

[49] S. Meghana, P. Kabra, S. Chakraborty, N. Padmavathy, Understanding the pathway of antibacterial activity of copper oxide nanoparticles, RSC Adv. 5 (2015) 12293–12299, https://doi.org/10.1039/c4ra12163e.

[50] M. Vincent, R.E. Duval, P. Hartemann, M. Engels-Deutsch, Contact killing and antimicrobial properties of copper, J. Appl. Microbiol. 124 (2018) 1032–1046, https://doi.org/10.1111/jam.13681.

[51] T. Ali, A. Ahmed, U. Alam, I. Uddin, P. Tripathi, M. Muneer, Enhanced photocatalytic and antibacterial activities of Ag-doped TiO_2 nanoparticles under visible light, Mater. Chem. Phys. 212 (2018) 325–335, https://doi.org/10.1016/j.matchemphys.2018.03.052.

[52] F. Ahmed, M.B. Kanoun, C. Awada, C. Jonin, P.F. Brevet, An experimental and theoretical study on the effect of silver nanoparticles concentration on the structural, morphological, optical, and electronic properties of tio_2 nanocrystals, Crystals 11 (2021), https://doi.org/10.3390/cryst11121488.

[53] K. Kayed, M. Issa, E. Alsoki, The band gap of silver nanoparticles in Ag/Ag2O composites synthesized by oxygen plasma treatment of silver thin films, Plasmonics 18 (2023) 711–717, https://doi.org/10.1007/s11468-023-01800-5.

[54] T.C. Dakal, A. Kumar, R.S. Majumdar, V. Yadav, Mechanistic basis of antimicrobial actions of silver nanoparticles, Front. Microbiol. 7 (2016) 1–17, https://doi.org/10.3389/fmicb.2016.01831.

[55] A. Roy, O. Bulut, S. Some, A.K. Mandal, M.D. Yilmaz, Green synthesis of silver nanoparticles: biomolecule-nanoparticle organizations targeting antimicrobial activity, RSC Adv. 9 (2019) 2673–2702, https://doi.org/10.1039/c8ra08982e.

[56] X. Fan, L. Yahia, E. Sacher, Antimicrobial properties of the Ag, Cu nanoparticle system, Biology 10 (2021) 1–37, https://doi.org/10.3390/biology10020137.

[57] Z. Ferdous, A. Nemmar, Health impact of silver nanoparticles: a review of the biodistribution and toxicity following various routes of exposure. https://doi.org/10.3390/ijms21072375, 2020.

[58] I.V. Vrček, I. Žuntar, R. Petlevski, I. Pavičić, M. Dutour Sikirić, M. Ćurlin, W. Goessler, Comparison of in vitro toxicity of silver ions and silver nanoparticles on human hepatoma cells, Environ. Toxicol. 31 (2016) 679–692, https://doi.org/10.1002/tox.22081.

[59] H. Chakhtouna, H. Benzeid, N. Zari, A. el kacem Qaiss, R. Bouhfid, Recent progress on Ag/TiO_2 photocatalysts: photocatalytic and bactericidal behaviors, Environ. Sci. Pollut. Control Ser. 28 (2021) 44638–44666, https://doi.org/10.1007/s11356-021-14996-y.

[60] M.P. Nikhila, D. John, M.R. Pai, N.K. Renuka, Cu and Ag modified mesoporous TiO [Formula presented] nanocuboids for visible light driven photocatalysis, Nano-Structures and Nano-Objects 21 (2020), https://doi.org/10.1016/j.nanoso.2019.100420.

[61] W. Mohammed, M. Matalkeh, R.M. Al Soubaihi, A. Elzatahry, K.M. Saoud, Visible light photocatalytic degradation of methylene blue dye and pharmaceutical wastes over ternary NiO/Ag/TiO_2 heterojunction, ACS Omega 8 (2023) 40063–40077. https://doi.org/10.1021/acsomega.3c01766.

[62] Z. Wei, M. Endo, K. Wang, E. Charbit, A. Markowska-Szczupak, B. Ohtani, E. Kowalska, Noble metal-modified octahedral anatase titania particles with enhanced activity for decomposition of chemical and microbiological pollutants, Chem. Eng. J. 318 (2017) 121–134, https://doi.org/10.1016/j.cej.2016.05.138.

[63] S.P. Tallósy, L. Janovák, E. Nagy, Á. Deák, Á. Juhász, E. Csapó, N. Buzás, I. Dékány, Adhesion and inactivation of Gram-negative and Gram-positive bacteria on photoreactive TiO_2/polymer and Ag–TiO_2 nanohybrid films, Appl. Surf. Sci. 371 (2016) 139–150, https://doi.org/10.1016/J.APSUSC.2016.02.202.

[64] M. Stucchi, C.L. Bianchi, C. Argirusis, V. Pifferi, B. Neppolian, G. Cerrato, D.C. Boffito, Ultrasound assisted synthesis of Ag-decorated TiO_2 active in visible light, Ultrason. Sonochem. 40 (2018) 282–288, https://doi.org/10.1016/J.ULTSONCH.2017.07.016.

[65] D.M. Tobaldi, C. Piccirillo, R.C. Pullar, A.F. Gualtieri, M.P. Seabra, P.M.L. Castro, J.A. Labrincha, Silver-modified nano-titania as an antibacterial agent and photocatalyst, J. Phys. Chem. C 118 (2014) 4751–4766, https://doi.org/10.1021/JP411997K/SUPPL_FILE/JP411997K_SI_001.PDF.

[66] Y. Cao, R. Wu, W. Zhang, J. Luo, Y. Li, L. Ning, R. Shen, D. Wang, W. Ye, Killing two birds with one stone: silver nanoparticles loaded on ultrathin N-doped carbon-coated TiO_2 porous spheres with narrow bandgap for efficient SERS sensing and photoinduced antibacterial applications, Appl. Surf. Sci. 583 (2022) 152512, https://doi.org/10.1016/J.APSUSC.2022.152512.

[67] K. Nanaji, R.K. Siri Kiran Janardhana, T.N. Rao, S. Anandan, Energy level matching for efficient charge transfer in Ag doped - Ag modified TiO_2 for enhanced visible light photocatalytic activity, J. Alloys Compd. 794 (2019) 662–671, https://doi.org/10.1016/J.JALLCOM.2019.04.283.

[68] M. Stucchi, C.L. Bianchi, C. Pirola, G. Cerrato, S. Morandi, C. Argirusis, G. Sourkouni, A. Naldoni, V. Capucci, Copper NPs decorated titania: a novel synthesis by high energy US with a study of the photocatalytic activity under visible light, Ultrason. Sonochem. 31 (2016) 295–301, https://doi.org/10.1016/J.ULTSONCH.2016.01.015.

[69] R. Kumar, S. Govindarajan, R.K. Siri Kiran Janardhana, T.N. Rao, S.V. Joshi, S. Anandan, Facile one-step route for the development of in situ cocatalyst-modified Ti3+ self-doped TiO_2 for improved visible-light photocatalytic activity, ACS Appl. Mater. Interfaces 8 (2016) 27642–27653, https://doi.org/10.1021/ACSAMI.6B07000/SUPPL_FILE/AM6B07000_SI_001.PDF.

[70] H.M. Yadav, S.V. Otari, V.B. Koli, S.S. Mali, C.K. Hong, S.H. Pawar, S.D. Delekar, Preparation and characterization of copper-doped anatase TiO_2 nanoparticles with visible light photocatalytic antibacterial activity, J. Photochem. Photobiol. Chem. 280 (2014) 32–38, https://doi.org/10.1016/J.JPHOTOCHEM.2014.02.006.

[71] V. Paramarta, A. Taufik, R. Saleh, Photocatalytic degradation of methylene blue (MB) by UV-light irradiation using SnO2/CeO2 modified nanographene platelets (NGP), in: J Phys Conf Ser, Institute of Physics Publishing, 2020, https://doi.org/10.1088/1742-6596/1442/1/012005.

[72] H. Liyanaarachchi, C. Thambiliyagodage, C. Liyanaarachchi, U. Samarakoon, Efficient photocatalysis of Cu doped TiO_2/g-C3N4 for the photodegradation of methylene blue, Arab. J. Chem. 16 (2023), https://doi.org/10.1016/j.arabjc.2023.104749.

[73] M. Theodosiou, E. Sakellis, N. Boukos, V. Kusigerski, B. Kalska-Szostko, E. Efthimiadou, Iron oxide nanoflowers encapsulated in thermosensitive fluorescent liposomes for hyperthermia treatment of lung adenocarcinoma, Sci. Rep. 12 (2022) 8697, https://doi.org/10.1038/s41598-022-12687-3.

[74] E. Eruslanov, S. Kusmartsev, Identification of ROS using oxidized DCFDA and flow-cytometry, in: D. Armstrong (Ed.), Advanced Protocols in Oxidative Stress III, Humana Press, a part of Springer Science + Business Media, 2010, pp. 1–477, https://doi.org/10.1007/978-1-60761-411-1.

[75] Y. Ren, X. Liu, R. Geng, Q. Lu, R. Rao, X. Tan, X. Yang, W. Liu, Increased level of α2,6-sialylated glycans on HaCaT cells induced by titanium dioxide nanoparticles under UV radiation, Nanomaterials 8 (2018) 1–14, https://doi.org/10.3390/nano8040253.

[76] T. Parandhaman, S.K. Das, Facile synthesis, biofilm disruption properties and biocompatibility study of a poly-cationic peptide functionalized graphene-silver nanocomposite, Biomater. Sci. 6 (2018) 3356–3372, https://doi.org/10.1039/c8bm01003j.

[77] B. Ramalingam, T. Parandhaman, S.K. Das, Antibacterial effects of biosynthesized silver nanoparticles on surface ultrastructure and nanomechanical properties of gram-negative bacteria viz. Escherichia coli and Pseudomonas aeruginosa, ACS Appl. Mater. Interfaces 8 (2016) 4963–4976, https://doi.org/10.1021/acsami.6b00161.

[78] F. Ahmed, M.B. Kanoun, C. Awada, C. Jonin, P.F. Brevet, An experimental and theoretical study on the effect of silver nanoparticles concentration on the structural, morphological, optical, and electronic properties of TiO_2 nanocrystals, Crystals 11 (2021), https://doi.org/10.3390/cryst11121488.

[79] F. Wang, S. Yang, Q. Lu, W. Liu, P. Sun, Q. Wang, W. Cao, Colloidal Cu-doped TiO_2 nanocrystals containing oxygen vacancies for highly-efficient photocatalytic degradation of benzene and antibacterial, Colloids Surf. A Physicochem. Eng. Asp. 658 (2023) 130741, https://doi.org/10.1016/j.colsurfa.2022.130741.

[80] A.S. Ethiraj, D.S. Rhen, A.V. Soldatov, G.A.M. Ali, Z.H. Bakr, Efficient and recyclable Cu incorporated TiO_2 nanoparticle catalyst for organic dye photodegradation, International Journal of Thin Film Science and Technology 10 (2021) 169–182, https://doi.org/10.18576/ijtfst/100306.

[81] M.A. Liaqat, Z. Hussain, Z. Khan, M.A. Akram, A. Shuja, Effects of Ag doping on compact TiO_2 thin films synthesized via one-step sol–gel route and deposited by spin coating technique, J. Mater. Sci. Mater. Electron. 31 (2020) 7172–7181, https://doi.org/10.1007/s10854-020-03288-9.

[82] X. Tao, P. Ruan, X. Zhang, H. Sun, X. Zhou, Microsphere assembly of TiO_2 mesoporous nanosheets with highly exposed (101) facets and application in a light-trapping quasi-solid-state dye-sensitized solar cell, Nanoscale 7 (2015) 3539–3547, https://doi.org/10.1039/c4nr06865c.

[83] B. Choudhury, M. Dey, A. Choudhury, Defect generation, d-d transition, and band gap reduction in Cu-doped TiO_2 nanoparticles, Int. Nano Lett. 3 (2013), https://doi.org/10.1186/2228-5326-3-25.

[84] J. Navas, A. Sánchez-Coronilla, T. Aguilar, N.C. Hernández, D.M. De Los Santos, J. Sánchez-Márquez, D. Zorrilla, C. Fernández-Lorenzo, R. Alcántara, J. Martín-Calleja, Experimental and theoretical study of the electronic properties of Cu-doped anatase TiO_2, Phys. Chem. Chem. Phys. 16 (2014) 3835–3845, https://doi.org/10.1039/c3cp54273d.

[85] S. Mathew, P. Ganguly, S. Rhatigan, V. Kumaravel, C. Byrne, S.J. Hinder, J. Bartlett, M. Nolan, S.C. Pillai, Cu-Doped TiO₂: visible light assisted photocatalytic antimicrobial activity, Appl. Sci. 8 (2018), https://doi.org/10.3390/app8112067.

[86] B. Rajamannan, S. Mugundan, G. Viruthagiri, P. Praveen, N. Shanmugam, Linear and nonlinear optical studies of bare and copper doped TiO 2 nanoparticles via sol gel technique, Spectrochim. Acta Mol. Biomol. Spectrosc. 118 (2014) 651–656, https://doi.org/10.1016/j.saa.2013.09.045.

[87] N. Lertthanaphol, N. Pienutsa, K. Chusri, T. Sornsuchat, P. Chanthara, P. Seeharaj, P. Kim-Lohsoontorn, S. Srinives, One-step hydrothermal synthesis of precious metal-doped titanium dioxide–graphene oxide composites for photocatalytic conversion of CO2 to ethanol, ACS Omega 6 (2021) 35769–35779, https://doi.org/10.1021/acsomega.1c05799.

[88] B. Rajamannan, S. Mugundan, G. Viruthagiri, P. Praveen, N. Shanmugam, Linear and nonlinear optical studies of bare and copper doped TiO 2 nanoparticles via sol gel technique, Spectrochim. Acta Mol. Biomol. Spectrosc. 118 (2014) 651–656, https://doi.org/10.1016/j.saa.2013.09.045.

[89] R.D. Desiati, M. Taspika, E. Sugiarti, Effect of calcination temperature on the antibacterial activity of TiO₂/Ag nanocomposite, Mater. Res. Express 6 (2019), https://doi.org/10.1088/2053-1591/ab155c.

[90] E.H. Alsharaeh, T. Bora, A. Soliman, F. Ahmed, G. Bharath, M.G. Ghoniem, K.M. Abu-Salah, J. Dutta, Sol-gel-assisted microwave-derived synthesis of anatase Ag/Tio2/Go nanohybrids toward efficient visible light phenol degradation, Catalysts 7 (2017), https://doi.org/10.3390/catal7050133.

[91] T.N. Rao, Riyazuddin, P. Babji, N. Ahmad, R.A. Khan, I. Hassan, S.A. Shahzad, F.M. Husain, Green synthesis and structural classification of Acacia nilotica mediated-silver doped titanium oxide (Ag/TiO₂) spherical nanoparticles: assessment of its antimicrobial and anticancer activity, Saudi J. Biol. Sci. 26 (2019) 1385–1391, https://doi.org/10.1016/j.sjbs.2019.09.005.

[92] M. Amiri, K. Dashtian, M. Ghaedi, S. Mosleh, A dual surface inorganic molecularly imprinted Bi2WO6-CuO/Ag2O heterostructure with enhanced activity-selectivity towards the photocatalytic degradation of target contaminants, Photochem. Photobiol. Sci. 19 (2020) 943–955, https://doi.org/10.1039/d0pp00008f.

[93] M.C. Biesinger, B.P. Payne, B.R. Hart, A.P. Grosvenor, N.S. McIntyre, L.W.M. Lau, R.S.C. Smart, Quantitative chemical state XPS analysis of first row transition metals, oxides and hydroxides, J Phys Conf Ser 100 (2008) 012025, https://doi.org/10.1088/1742-6596/100/1/012025.

[94] M.J. Islam, M. Granollers Mesa, A. Osatiashtiani, J.C. Manayil, M.A. Isaacs, M.J. Taylor, S. Tsatsos, G. Kyriakou, PdCu single atom alloys supported on alumina for the selective hydrogenation of furfural, Appl. Catal., B 299 (2021) 120652, https://doi.org/10.1016/J.APCATB.2021.120652.

[95] M.C. Biesinger, Advanced analysis of copper X-ray photoelectron spectra, Surf. Interface Anal. 49 (2017) 1325–1334, https://doi.org/10.1002/SIA.6239.

[96] S. Tsatsos, G. Kyriakou, Copper growth on a stepped nickel surface: electronic and geometric effects on CO reactivity, J. Phys. Chem. C 127 (2023) 6337–6346, https://doi.org/10.1021/ACS.JPCC.3C00377/ASSET/IMAGES/LARGE/JP3C00377_0006.JPEG.

[97] S.W. Gaarenstroom, N. Winograd, Initial and final state effects in the ESCA spectra of cadmium and silver oxides, J. Chem. Phys. 67 (1977) 3500–3506, https://doi.org/10.1063/1.435347.

[98] G.B. Hoflund, Z.F. Hazos, G.N. Salaita, Surface characterization study of Ag, AgO, and Ag₂O using x-ray photoelectron spectroscopy and electron energy-loss spectroscopy, Phys. Rev. B 62 (2000) 11126, https://doi.org/10.1103/PhysRevB.62.11126.

[99] I.S. Grover, S. Singh, B. Pal, The preparation, surface structure, zeta potential, surface charge density and photocatalytic activity of TiO 2 nanostructures of different shapes, Appl. Surf. Sci. 280 (2013) 366–372, https://doi.org/10.1016/j.apsusc.2013.04.163.

[100] D.L. Liao, G.S. Wu, B.Q. Liao, Zeta potential of shape-controlled TiO₂ nanoparticles with surfactants, Colloids Surf. A Physicochem. Eng. Asp. 348 (2009) 270–275, https://doi.org/10.1016/j.colsurfa.2009.07.036.

[101] K. Suttiponparnit, J. Jiang, M. Sahu, S. Suvachittanont, T. Charinpanitkul, P. Biswas, Role of surface area, primary particle size, and crystal phase on titanium dioxide nanoparticle dispersion properties, Nanoscale Res. Lett. 6 (2011) 1–8, https://doi.org/10.1007/s11671-010-9772-1.

[102] M. Miyauchi, H. Irie, M. Liu, X. Qiu, H. Yu, K. Sunada, K. Hashimoto, Visible-light-Sensitive photocatalysts: nanocluster-grafted titanium dioxide for indoor environmental remediation, J. Phys. Chem. Lett. 7 (2016) 75–84, https://doi.org/10.1021/acs.jpclett.5b02041.

[103] M. Janczarek, E. Kowalska, On the origin of enhanced photocatalytic activity of copper-modified titania in the oxidative reaction systems, Catalysts 7 (2017) 317, https://doi.org/10.3390/CATAL7110317, 7 (2017) 317.

[104] Y. Xia, Z. He, J. Su, K. Hu, Construction of novel Cu 2 O/PbBiO 2 Br composites with enhanced photocatalytic activity, J. Mater. Sci. Mater. Electron. 30 (2019) 9843–9854, https://doi.org/10.1007/S10854-019-01321-0/FIGURES/12.

[105] G. Colón, M. Maicu, M.C. Hidalgo, J.A. Navío, Cu-doped TiO₂ systems with improved photocatalytic activity, Appl. Catal., B 67 (2006) 41–51, https://doi.org/10.1016/j.apcatb.2006.03.019.

[106] B. Choudhury, A. Choudhury, Oxygen defect dependent variation of band gap, Urbach energy and luminescence property of anatase, anatase-rutile mixed phase and of rutile phases of TiO₂ nanoparticles, Physica E Low Dimens Syst Nanostruct 56 (2014) 364–371, https://doi.org/10.1016/j.physe.2013.10.014.

[107] B. Choudhury, A. Choudhury, Oxygen defect dependent variation of band gap, Urbach energy and luminescence property of anatase, anatase-rutile mixed phase and of rutile phases of TiO₂ nanoparticles, Physica E Low Dimens Syst Nanostruct 56 (2014) 364–371, https://doi.org/10.1016/j.physe.2013.10.014.

[108] H. Irie, S. Miura, K. Kamiya, K. Hashimoto, Efficient visible light-sensitive photocatalysts: grafting Cu(II) ions onto TiO₂ and WO3 photocatalysts, Chem. Phys. Lett. 457 (2008) 202–205, https://doi.org/10.1016/j.cplett.2008.04.006.

[109] O.V. Komova, A.V. Simakov, V.A. Rogov, D.I. Kochubei, G.V. Odegova, V.V. Kriventsov, E.A. Paukshtis, V.A. Ushakov, N.N. Sazonova, T.A. Nikoro, Investigation of the state of copper in supported copper-titanium oxide catalysts, J. Mol. Catal. Chem. 161 (2000) 191–204, https://doi.org/10.1016/S1381-1169(00)00342-3.

[110] G. Li, N.M. Dimitrijevic, L. Chen, T. Rajh, K.A. Gray, Role of surface/interfacial Cu2+ sites in the photocatalytic activity of coupled CuO-TiO₂ nanocomposites, J. Phys. Chem. C 112 (2008) 19040–19044, https://doi.org/10.1021/jp8068392.

[111] D.V. Ponnuvelu, B. Pullithadathil, A.K. Prasad, S. Dhara, K. Mohamed, A.K. Tyagi, B. Raj, Highly sensitive, atmospheric pressure operatable sensor based on Au nanoclusters decorated TiO2@Au heterojunction nanorods for trace level NO2 gas detection, J. Mater. Sci. Mater. Electron. 28 (2017) 9738–9748, https://doi.org/10.1007/s10854-017-6725-9.

[112] K. Xie, C. Gong, M. Wang, L. Sun, C. Lin, Tuning Ag morphology on TiO₂ nanotube arrays by pulse reverse current deposition for enhanced plasmon-driven visible-light response, J. Appl. Electrochem. 47 (2017) 959–968, https://doi.org/10.1007/s10800-017-1093-y.

[113] Y. Li, Q. Liao, W. Hou, L. Qin, Silver-based surface plasmon sensors: fabrication and applications, Int. J. Mol. Sci. 24 (2023), https://doi.org/10.3390/ijms24044142.

[114] E. Grabowska, A. Zaleska, S. Sorgues, M. Kunst, A. Etcheberry, C. Colbeau-Justin, H. Remita, Modification of titanium(IV) dioxide with small silver nanoparticles: application in photocatalysis, J. Phys. Chem. C 117 (2013) 1955–1962, https://doi.org/10.1021/jp3112183.

[115] P. Makuła, M. Pacia, W. Macyk, How to correctly determine the band gap energy of modified semiconductor photocatalysts based on UV-vis spectra, J. Phys. Chem. Lett. 9 (2018) 6814–6817, https://doi.org/10.1021/acs.jpclett.8b02892.

[116] S. Moosavi, R.Y.M. Li, C.W. Lai, Y. Yusof, S. Gan, O. Akbarzadeh, Z.Z. Chowhury, X.G. Yue, M.R. Johan, Methylene blue dye photocatalytic degradation over synthesised fe3 o4/ac/tio2 nano-catalyst: degradation and reusability studies, Nanomaterials 10 (2020) 1–15, https://doi.org/10.3390/nano10122360.

[117] Y. Mingmongkol, D.T.T. Trinh, P. Phuinthiang, D. Channei, K. Ratananikom, A. Nakaruk, W. Khanitchaidecha, Enhanced photocatalytic and photokilling activities of Cu-doped TiO₂ nanoparticles, Nanomaterials 12 (2022), https://doi.org/10.3390/nano12071198.

[118] B. Choudhury, M. Dey, A. Choudhury, Shallow and deep trap emission and luminescence quenching of TiO₂ nanoparticles on Cu doping, Appl. Nanosci. 4 (2014) 499–506, https://doi.org/10.1007/s13204-013-0226-9.

[119] M.G. Méndez-Medrano, E. Kowalska, A. Lehoux, A. Herissan, B. Ohtani, D. Bahena, V. Briois, C. Colbeau-Justin, J.L. Rodríguez-López, H. Remita, Surface modification of TiO₂ with Ag nanoparticles and CuO nanoclusters for application in photocatalysis, J. Phys. Chem. C 120 (2016) 5143–5154, https://doi.org/10.1021/acs.jpcc.5b10703.

[120] P. Activity, H. Nishikiori, N. Harata, S. Yamaguchi, T. Ishikawa, Formation of CuO on TiO 2 Surface Using its, 2019, pp. 1–12.

[121] Y. Ding, I.S. Yang, Z. Li, X. Xia, W.I. Lee, S. Dai, D.W. Bahnemann, J.H. Pan, Nanoporous TiO₂ spheres with tailored textural properties: controllable synthesis, formation mechanism, and photochemical applications, Prog. Mater. Sci. 109 (2020) 100620, https://doi.org/10.1016/j.pmatsci.2019.100620.

[122] N. Norouzi, A.C. Nusantara, Y. Ong, T. Hamoh, L. Nie, A. Morita, Y. Zhang, A. Mzyk, R. Schirhagl, Relaxometry for detecting free radical generation during Bacteria's response to antibiotics, Carbon N Y 199 (2022) 444–452, https://doi.org/10.1016/j.carbon.2022.08.025.

[123] E. Eruslanov, S. Kusmartsev, Identification of ROS using oxidized DCFDA and flow-cytometry, in: D. Armstrong (Ed.), Advanced Protocols in Oxidative Stress III, Humana Press, a part of Springer Science + Business Media, 2010, pp. 1–477, https://doi.org/10.1007/978-1-60761-411-1.

[124] W.I. Abdel-Fatah, M.M. Gobara, S.F.M. Mustafa, G.W. Ali, O.W. Guirguis, Role of silver nanoparticles in imparting antimicrobial activity of titanium dioxide, Mater. Lett. 179 (2016) 190–193, https://doi.org/10.1016/j.matlet.2016.05.063.